Electrostatic turbulent structures in TORPEX plasmas

Diploma Thesis

Christian Theiler

Under supervision of

Prof. A. Fasoli
Dr. I. Furno
EPFL-CRPP

Prof. A. Benz
Institute of Astronomy
ETH Zürich

February 2007

Abstract

Experimental data from many Tokamaks suggest that an important fraction of radial particle and heat transport in the Scrape-Off-Layer is due to poloidally-localized propagating structures of increased plasma density (blobs). A better understanding of the mechanism leading to blobs might help to lower the radial transport and control damages to plasma facing components. Such structures are experimentally investigated in the basic toroidal device TORPEX. Ion saturation current measurements from a two-dimensional imaging probe are analyzed using conditional sampling (CS). This technique is extensively studied and a large variety of trigger conditions is used to detect coherent structures in the turbulent plasma. Two scenarios are observed which lead to the ejection of blobs. The role of the density gradient in the blob ejection mechanism is investigated. In a first step, the evolution of the gradients leading to blobs is studied by triggering on such events. Their magnitude increases with the size of the blob. In a second step, these gradients are used directly as reference signals for CS. Strong gradients are found to have an enhanced probability to give rise to a blob. The location of the source before a possible blob ejection is also determined. It is concluded that the effect of the source is to steepen up the gradient in a uniform way along the vertical direction.

Contents

1

Introduction

Nuclear Fusion

Nuclear fusion, the energy source of the stars, is a promising option for a long-term, safe, environmentally friendly and economically competitive energy source. The most promising fusion reaction in the laboratory is

$$D + T \rightarrow He(3.52MeV) + n(14.1MeV) \tag{1.1}$$

due to its relatively large fusion cross-section. Deuterium (D) is abundant in nature, whereas Tritium (T) is unstable, with a half-live of 12.3 years. It can be produced by the reaction

$$^6Li + n \rightarrow \ ^4He + 4.8MeV + T \tag{1.2}$$

and Lithium (Li) can be extracted from sea water. In order to induce the reaction (1.1), the energy of D and T must be sufficiently high to overcome the repulsive Coulomb barrier between them. A gas consisting of such energetic particles is completely ionized and forms a plasma. A plasma is an ensemble of charged particles with many interesting properties. It can shield out electrostatic perturbations within short distances, there are many different sorts of waves which can propagate through a plasma and it produces many beautiful phenomena in nature (aurora, cosmic nebula,...). Although a plasma is often associated with very high temperatures, it can range over many orders of magnitude in both temperature and density (see Fig. 1.1).

To run a fusion reactor efficiently, the plasma needs to be confined under extreme conditions. The Lawson criterion [19] gives a rough estimate of the required plasma parameters. It assumes a reactor where the energy losses of the plasma are equilibrated by an external heating. The

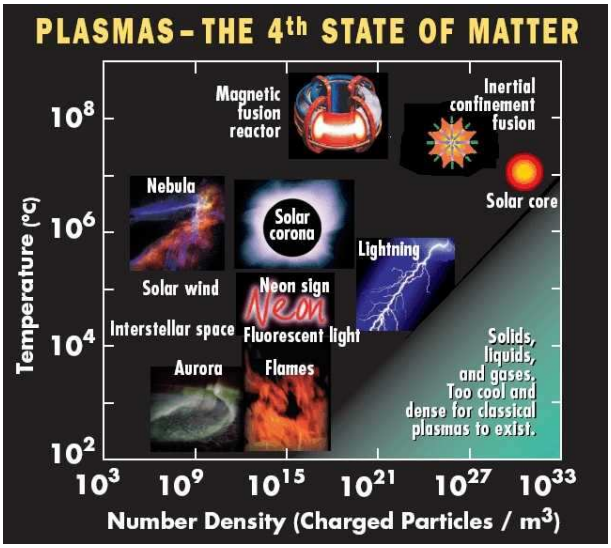

Figure 1.1: An overview of different plasmas and corresponding temperatures and densities.

power leaving the plasma is converted to electrical power. This power should of course be larger than what is needed for the plasma heating. For this to be the case, the product $n\tau_E$ of the particle density n and the energy confinement time τ_E of the plasma has to exceed a value of around $5 \times 10^{19}\mathrm{m}^{-3}\mathrm{s}$ and this at a temperature of about $2 \times 10^8\mathrm{K}$. There is an optimal value for the temperature. For $n\tau_E$ fixed, the fusion power becomes too small for low temperatures. For T very high, the losses increase faster with temperature than the fusion power.

Single particle picture of plasma confinement

While the plasma in the stars is confined through gravitational forces, magnetic field configurations can be used to do this in the laboratory.
A first idea of this confinement can be obtained from a single-particle picture. In a homogeneous magnetic field $\mathbf{B}$, a single charged particle is forced to spiral around a field line and can only propagate freely in the direction parallel to B. It thus essentially stays along the same field line. This is no longer true in a toroidal magnetic field. If the variations of $\mathbf{B}$ are small within the radial excursions of the charged particle from its initial field line, the particle will, in addition to its gyration around the field line, have a drift approximately given by

$$\mathbf{V}_D = \frac{m}{q}\frac{1}{R^2B^2}(\mathbf{R} \wedge \mathbf{B})\left\{ v_\parallel^2 + \frac{1}{2}v_\perp^2 \right\}, \tag{1.3}$$

where $\mathbf{R}$ is the radius-of-curvature of the magnetic field $\mathbf{B}$, m the mass of the particle, q its charge and v its velocity. This effect is illustrated in Fig. 1.2. There, 0.05 ms of the trajectory of an electron in a curved magnetic field is shown for typical parameters of TORPEX, i.e a magnetic field of 70 mT at a distance of 1 m and an electron energy of about 2 eV [4]. From this, it becomes clear that a purely toroidal magnetic field can not provide a good confinement of the plasma. Since the drift in equation (1.3) is charge dependent, electrons and ions have a drift in opposite direction. This leads to charge separation and thus a vertical electric field $\mathbf{E}$,

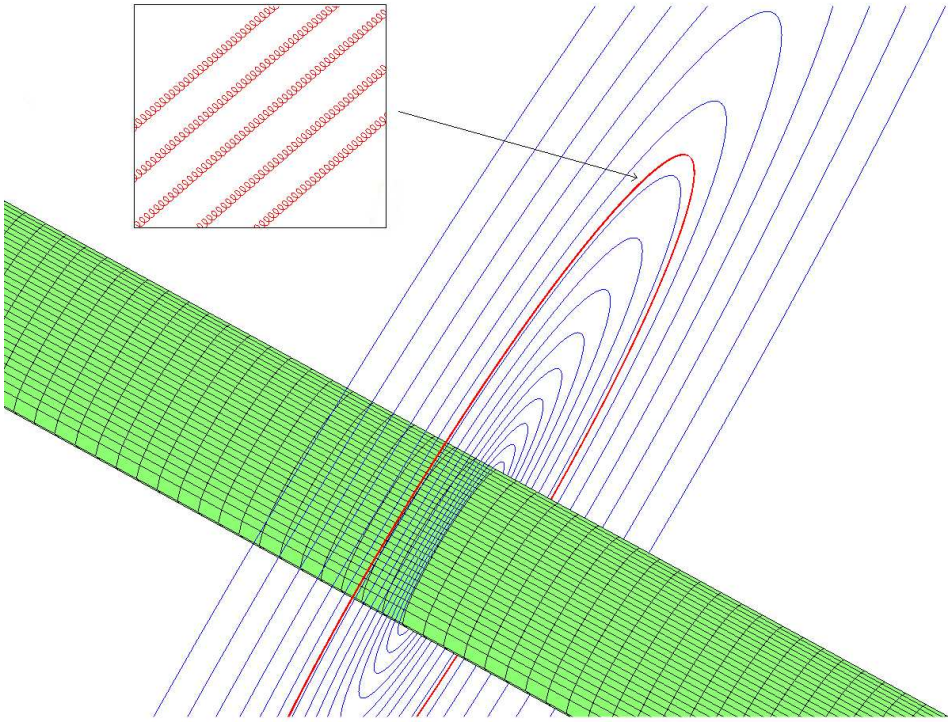

Figure 1.2: The trajectory of an electron in a curved magnetic field is shown. Such a field could in principle be produced by a current in a straight wire (green cylinder). From far away, the electron seems to follow perfectly the magnetic field lines (blue circles). As one goes closer, one sees that the electron does not return exactly to the same position after one turn around the wire. It has moved a little parallel to the wire, in agreement with (1.3). (Figure produced with Matlab using classical forth-order Runge-Kutta).

i.e. a field parallel to the symmetry axis of the torus. This electric field gives rise to a $\mathbf{E} \times \mathbf{B}$ drift

$$\mathbf{V}_{\mathbf{E}\times\mathbf{B}} = \frac{\mathbf{E} \times \mathbf{B}}{B^2} \tag{1.4}$$

and therefore a strong particle loss in the radial direction.
The particle drifts can be compensated by a helical twist of the field lines. This is achieved by adding a poloidal component to a toroidal magnetic field. In Stellarators, this poloidal field is produced by external coils. In Tokamaks, it is achieved by a toroidal current in the plasma, which is induced by a transformer. In the case of a Tokamak, a vertical field component is needed as well to counteract the expanding force the plasma ring produces on itself.

Motivation

It is clear that such a confinement is not perfect. Due to Coulomb collisions between unlike particles, diffusion of the plasma opposing the density gradient and a resulting particle transport across the field lines is to be expected. The diffusion coefficient D indicates the importance of this transport. It is the product of the collision frequency and the square of the step size,

i.e. the distance particles travel in between/as a consequence of a collision. In a homogeneous field, the step size is of the order of the Larmor radius. This step size can be considerably larger in more complex magnetic field configurations, where particles follow complicated orbits. But still, the experimentally measured transverse transport is usually much larger than predicted by collisional theories. This phenomenon is called anomalous transport. It is believed that low-frequency electrostatic instabilities driven by density and temperature gradients and resulting plasma turbulence are responsible for this enhanced level of transport. The physical mechanism of such an instability, the flute instability, is illustrated in Fig. 1.3. It is driven by a charge independent force $\mathbf{F}$, which opposes the density gradient of a plasma supported by a magnetic field. This force can be gravitation, but also be due to magnetic field gradients and curvature. In the second case, the flute mode is often called interchange mode. In a linear regime, such instabilities produce a continuous particle transport across the confining field.
In the Scrape-Off-Layer of various Tokamaks, plasma blobs, i.e. poloidally-localized regions of increased plasma density, have been observed. This suggests that a significant fraction of transverse transport is due to these large intermittent events. A better understanding of the mechanism leading to blobs might help to lower the radial transport and control damages to plasma facing components.
There are several computing models for blob generation and propagation [1], but a deeper understanding and experimental verification is hampered by insufficient diagnostic access in fusion devices. This difficulty is overcome in the basic plasma experiment TORPEX, a toroidal device operating since march 2003, which is dedicated to the study of plasma turbulence and transport. There, plasmas of low enough temperatures and densities are produced which permit high spatial and temporal resolution measurements over the entire cross-section of the device. This allows to study both formation and propagation of blobs. Although it is not always evident how to extrapolate from a basic experiment to the Tokamak situation, TORPEX contains the main ingredients for turbulence relevant for fusion experiments such as gradients in the plasma profile and a curved magnetic field. In addition, several important dimensionless parameters fall in the same range both for Tokamaks and basic devices [18].
For the study of blobs, a statistical analysis techniques has recently been developed for TORPEX, which allows to describe structure dynamics in terms of probability distributions of object-related random variables, such as structure speed, size etc. [6]. Another approach is the conditional sampling (CS) technique, which uses a trigger condition on an external signal to identify coherent structures. It is the main method applied in this work.

Outline of the thesis

In the following, intermittent transport in TORPEX plasmas is studied by the use of ion saturation current measurements from a two-dimensional imaging probe. The experimental technique is introduced in chapter 2. Chapter 3 describes the TORPEX device and the target plasma. The plasma dynamics are analyzed in chapter 4. Comparison with earlier results from another diagnostic in 4.1 is followed by an investigation of the trigger condition. Different locations for blob detection are studied in 4.3. The role of density gradients in the blob ejection is investigated in section 4.4. This is done for two different positions of blob arrival, in a first step by triggering on the blob signal and afterwards by triggering on the local gradient directly. In 4.5, the location of the source is experimentally determined for events that are likely to eject a blob.

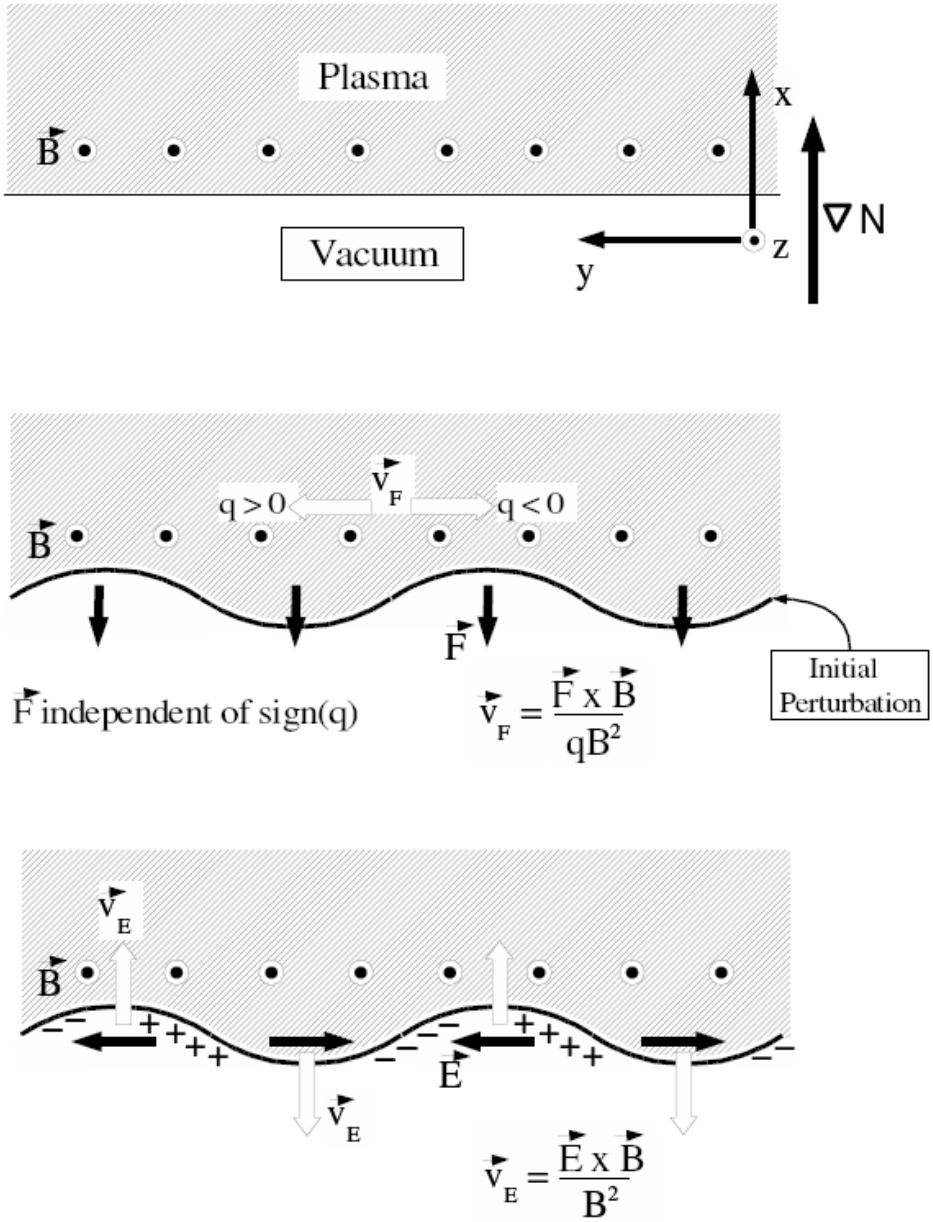

Figure 1.3: The basic mechanism of the flute instability is shown. A magnetized plasma is assumed with a density gradient in the x-direction. If there is a charge independent force $\mathbf{F}$ that opposes the density gradient, an initial perturbation will be reinforced. $\mathbf{F}$ gives rise to a charge dependent drift $V_{\mathbf{F}}$ and a charge accumulation due to the inhomogenity in the y-direction. The result is an electric field and an $\mathbf{E} \times \mathbf{B}$ drift which is directed such a way that it amplifies the perturbation. If $\mathbf{F}$ were in the same direction as the density gradient, charge separation would happen the other way around and the $\mathbf{E} \times \mathbf{B}$ drift would damp the initial perturbation (graphic taken from [3]).

2

Conditional sampling technique

Conditional sampling (CS) is a widely used method to extract large-scale coherent structures in turbulent plasmas and neutral fluids [10] [5] [11]. Spatio-temporal profiles of these structures can be obtained with high resolution by the use of only two probes. In this chapter, I want to present this quite simple method and apply it to synthetic data to become familiar with it and already get an idea of its limitations.

The following scenario is assumed. One deals with a fluctuating equilibrium, i.e. a turbulent state with stationary mean values. Let $f(x,t)$ be a spatio-temporal signal, for example the particle density. Suppose that $f(x,t)$ consists of an incoherently fluctuating part together with intermittently occurring coherent structures such as for example a fast growing mode. The average spatio-temporal evolution of such a structure can be found using conditional sampling. One probe at a fixed position x_{ref} is needed to detect the occurrence of the coherent structure. This is done by defining an appropriate trigger condition. For every triggered event, a sequence of given length is taken out of a simultaneously measured signal at a movable position x_{mov}. Finally, the average is taken over all these sequences. By repeating this procedure for different positions of the movable probe, the average evolution of the coherent structure can be found with high spatial resolution.

I would like to illustrate this by the use of synthetic data generated in a similar way as in [2]. For the signal at x_{ref} and x_{mov}, time series of 10^5 samples and Gaussian distributed noise with a standard deviation $\sigma = 0.2$ are taken. 500 randomly distributed coherent structures are added with the only constraint that they do not overlap. The form of the coherent structures chosen for x_{ref} and x_{mov} are shown in Fig. 2.1 (a) and (b), respectively. Since the structures at x_{ref} and x_{mov} are assumed to belong to the same large coherent structure, they are not independent of each other but appear in a fixed time relation. A way to select the coherent structures in $f(x_{ref},t)$ is to scan it for local maxima larger then a defined threshold value. In Fig. 2.1(c), part of the signal at x_{ref} is shown. The points satisfying the trigger condition are marked by

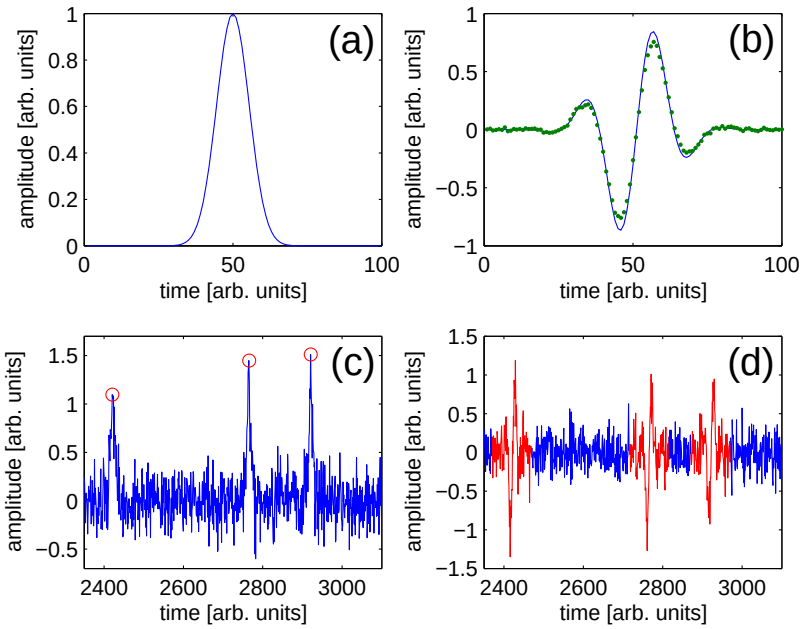

Figure 2.1: Conditional sampling is applied to synthetic data. In (a), the coherent structure from the signal at x_{ref} is shown. The one at x_{mov} together with the CS-result (green dots) is shown in (b). In (c), part of the signal at x_{ref} is shown. The triggered events are marked by red circles. (d) shows the corresponding part at x_{mov}. The red sequences are the selected windows used for the averaging.

red circles. In Fig. 2.1(d) we see the corresponding sequence at x_{mov}. In red, the sequences are shown which are cut out and over which the average is taken. The result of the conditional sampling is visible in Fig. 2.1(b) (green dots). It is the average of 489 trigger events.

The result of conditional sampling is an estimate for the conditional average

$$\langle f \rangle_{ca}(x,\tau) = \langle f(x,t+\tau)|C(f(x_{ref},t))\rangle, \tag{2.1}$$

where angular brackets denote ensemble averages and C is the condition on the signal at the reference probe, i.e. the trigger condition. $\langle f \rangle_{ca}(x,\tau)$ is the average value of the observable at x under the constraint that it satisfies condition C at x_{ref} τ time units before.

Of course, whether or not $\langle f \rangle_{ca}(x,\tau)$ gives any interesting physical insights depends crucially on the choice of the condition C. In this first example, a threshold was sufficient to retrieve the coherent structure. However, if the noise level is raised to $\sigma = 0.6$, the result becomes worse (see Fig. 2.2). It has the right qualitative shape but there is a strong loss in amplitude. This loss is due to two reasons. First, there are random fluctuations which are larger then the threshold value and thus give a trigger event, event hough there is no coherent structure present. In this simulation, 167 of 516 triggers were of this kind. Since they give essentially a random contribution to the average, their effect is to decrease the amplitude of the CS-signal. The second reason is that the 349 triggers which actually belong to a coherent structure are dispersed around the exact time of its occurrence. The shape of the signal in Fig. 2.1 (a) is changed considerably by the noise and the detected maximum does therefore not need to be the

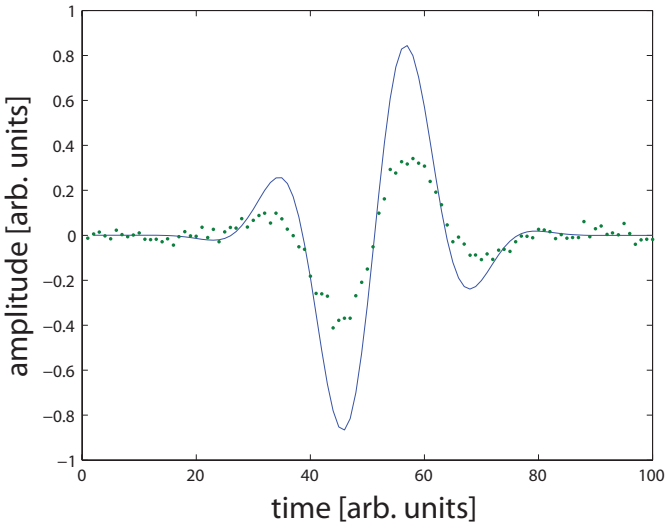

Figure 2.2: Original structure (blue line) together with the CS-result (green dots) for a large level of noise. An important loss in amplitude is visible.

maximum of the original structure. This leads to a washing out of the CS-signal and thus also to a loss in amplitude. The same effect already lead to a small amplitude loss in the first example with a lower noise level (Fig. 2.1 (b)).

So far in these very simplified examples, the conditional average has given at least qualitatively the 'physics' contained in the signal at x_{mov}. A more problematic situation arises, if there are two different coherent structures present in the fluctuation and if the trigger condition is not specific enough to make a distinction between the two. In such a case, conditional sampling gives an average of the two. This is illustrated in Fig. 2.3. The signal at x_{mov} has been generated by randomly distributing two different coherent structures (blue and red curve in Fig. 2.3), 250 times each, along a time series of 10^5 samples and Gaussian distributed noise with a standard deviation $\sigma = 0.2$ has been added. The signal at x_{ref} was generated in a similar way but with coherent structures that can not be distinguished by a threshold as a trigger condition. The result is shown in Fig. 2.3 (green dots). To compare, the average of the two coherent structures at x_{ref} is also shown (green solid line).

When working with real date, it is not clear from the start that structures which appear repeatedly in the signal at x_{ref} are related in any way to what happens at x_{mov}. If there is no relation and enough events are triggered, conditional sampling gives something essentially constant. So, a non-trivial result already indicates a correlation. To get a better quantitative idea of how good this correlation is, it can be useful to see how much the individual triggered sequences vary from the average. A good parameter for this is the standard deviation. In Fig. 2.4, top row, the CS-result of the three previous examples is shown again together with the σ-band. Meaning that for each time sample, the distance between the green and the red curve is the standard deviation of the distribution of all the values which have contributed to the average. In the bottom line of Fig. 2.4, the standard deviation is plotted alone. The peaks in the first graph correspond to the biggest slopes of the coherent structure. There, small deviations of the trigger time from the exact occurrence time of the structure have the biggest effect. In the second one, these deviations are bigger and the peaks are washed out. In the third one, the large peaks are due to the fact that there were two different structures contributing to the average.

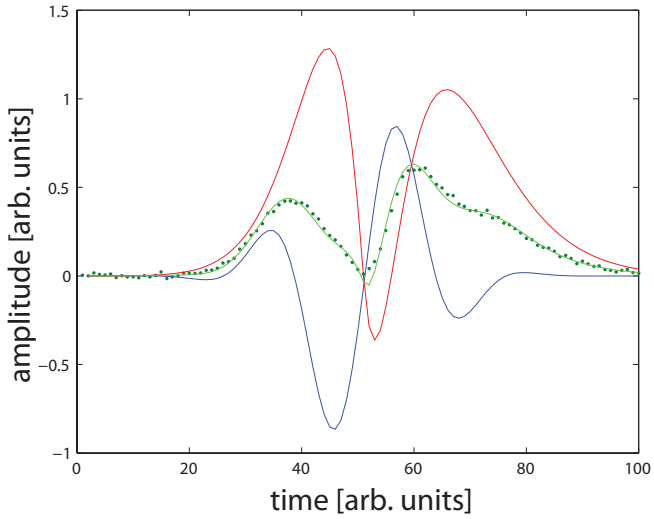

Figure 2.3: The case of two coherent structures is considered which both give rise to trigger events at x_{ref}, and equally often. The red and blue line show the form of the two structures, the green line their average and the green dots the result from the conditional sampling.

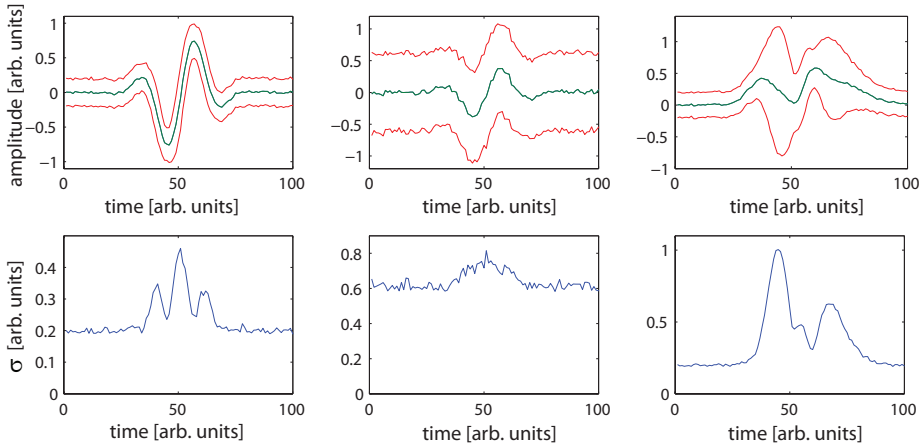

Figure 2.4: In the top row, the CS-results of the three previous examples are shown again, together with the σ-band. In the bottom row, $\sigma(t)$ is plotted alone.

3

Experimental setup

In this chapter, the TORPEX device is presented. The basic physics governing plasma production and confinement are briefly discussed, as well as the diagnostics relevant for this work. In the second part, the target plasma is specified and results prior to this thesis are reviewed.

3.1 The TORPEX device

The TORPEX experiment is shown in Fig. 3.1. Its main part is the vacuum vessel with major and minor radius of 1 m and 0.2 m. It has movable sectors as well as openings where different devices such as antennas and probes can be installed. Flow-meters allow adjusting the injection rate of different gases. Toroidal coils are installed to generate a toroidal field up to 0.1 Tesla. Horizontal coils allow for a vertical field component up to around 5 mT as well as for the induction of a loop voltage. A microwave source is installed for the production and sustainment of the plasma. It produces microwaves of 2.45 GHz, which corresponds to the electron cyclotron range of frequencies. The power can be adjusted between 0.2 and 20 kW. It can be modulated for sinusoidal, square and triangle waveforms.
These control parameters allow the production of highly reproducible H, He and Ar plasmas with density, electron temperature, and plasma potential in the range $n_e \approx 10^{16} - 10^{17}$ m^{-3} , $T_e \approx 5 - 10$ eV and $V_p \approx 10 - 20$ V .

3.1.1 Plasma production

In TORPEX, the plasma is produced and sustained by injection of microwaves perpendicular to the magnetic field from the low field side (LFS). Before the plasma is formed, the naturally ex-

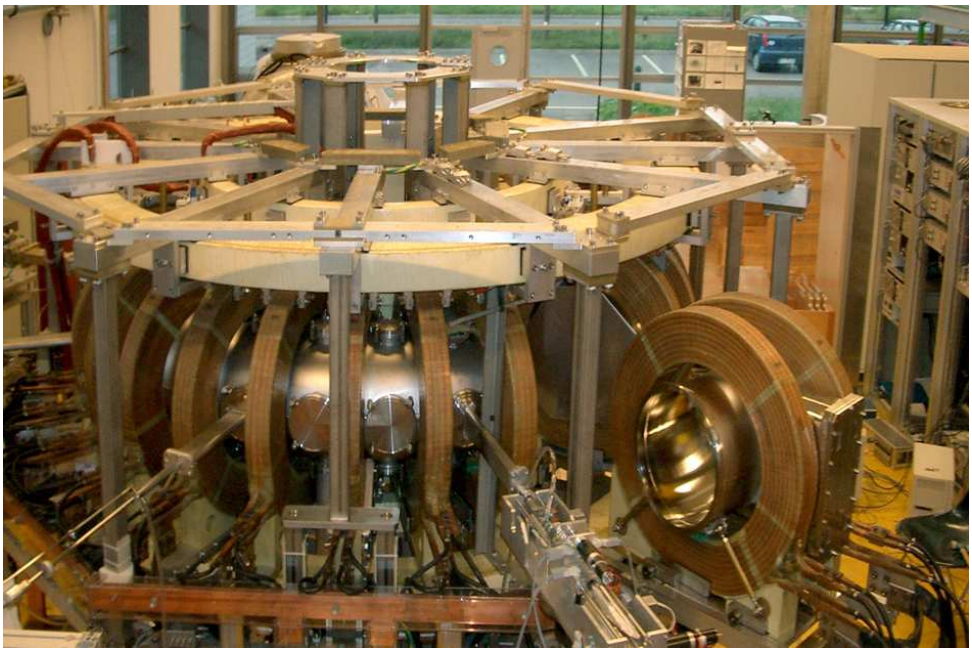

Figure 3.1: The TORPEX experiment

isting free electrons are accelerated, most efficiently at the elecron cyclotron (EC) layer, where the electron cyclotron frequency ω_c is equal to the microwave frequency ω_{rf}. Impact ionisation occurs and the plasma is formed. To sustain the plasma, the wave is injected in the O-mode polarization to avoid the cutoff of the X-mode [15]. After reflection on the high field side (HFS) wall, both O-mode and X-mode waves propagate back in the plasma. It has been shown [13] that the most energy is absorbed at the upper hybrid (UH) layer, where the X-mode encounters a fluid plasma resonance. The UH layer lies at a position where

$$\frac{ne^2}{\epsilon_0 m_e} + \frac{e^2 B^2}{m_e^2} = \omega_{rf}^2. \tag{3.1}$$

B is the magnitude of the magnetic field, e and m_e the electron charge and mass, respectively, n the electron density and ϵ_0 the permittivity of free space. The UH layer lies thus more to the LFS than the EC layer, where also part of the energy is deposited [13]. When the injected microwave power is increased, the plasma density increases and the UH layer moves further towards the LFS [8].

3.1.2 Plasma confinement

As we have seen in section 1, a simple toroidal plasma is not in equilibrium. Charge-dependent particle drifts give rise to a vertical electric field and therefore a radial $\mathbf{E} \times \mathbf{B}$ drift. Adding a vertical field component B_z allows to lower the electric field due to currents parallel to the open magnetic field lines (see Fig. 3.2). This results in a much better confinement of the plasma. A higher B_z allows for a better compensation of the electric field, but leads to an enhanced particle loss where the magnetic field lines intersect the vacuum vessel. It has been shown theoretically and experimentally that there is an optimal value for B_z, which maximizes the confinement

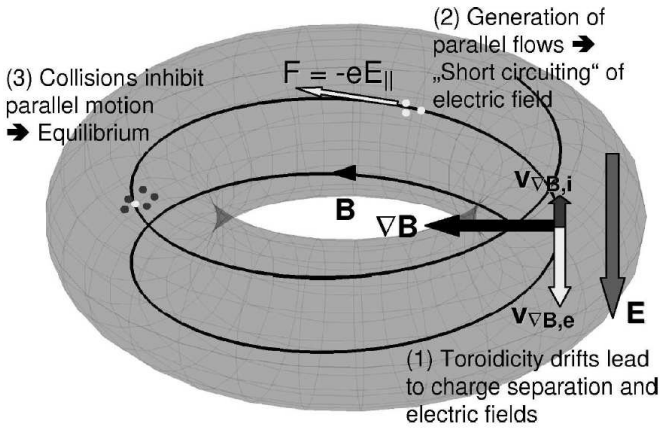

Figure 3.2: Visualization of the confinement principle of TORPEX. Charge separation due to curvature drifts gives rise to a vertical electric field. This field is partly compensated by currents along the magnetic field lines (graphic taken from [8]) .

time τ_E [9]. For a toroidal field of $B_\phi = 0.0766$ T, the optimal B_z is ~ 0.6 mT and gives a confinement time of $\tau_E \sim 0.6$ ms .

3.1.3 Langmuir probes

Most measurements on TORPEX are performed by the use of Langmuir probes. Usually, this are wires isolated up to a small pin at the end, which are held into the plasma. They measure the floating potential V_{fl}, i.e. the voltage at zero current, or the current drawn from the plasma as a response to a bias voltage V. A theoretical model is needed to translate these measurements to physical quantities. For TORPEX, the following model is used [17]

$$I(V) = \frac{1}{2} en \sqrt{\frac{T_e}{m_i}} A_\perp \left(1 - exp\left(\frac{V - V_{fl}}{T_e}\right)\right), \tag{3.2}$$

where $A_\perp$ is the area of the projection of the probe pin parallel to the magnetic field. The plasma potential V_{pl} is obtained from $V_{pl} = V_{fl} + \mu T_e/e$, where μ is an experimentally determined coefficient [13]. Mean values of the plasma potential, the electron temperature and the density can be obtained by sweeping the applied voltage in a triangular waveform and fitting the curve $I(V)$, obtained by averaging over several sweeping cycles, to the model described by Eq. (3.2). Time resolved profiles can be reconstructed using boxcar averaging techniques [12]. This has shown that it is often reasonable to set

$$n \propto I_{sat} = \frac{1}{2} en \sqrt{\frac{T_e}{m_i}} A_\perp, \tag{3.3}$$

and thus neglecting the dependence on T_e. The ion saturation current I_{sat} is measured by applying a strong negative bias voltage to the probe. Less reliable is the interpretation of V_{fl} as the plasma potential V_p.

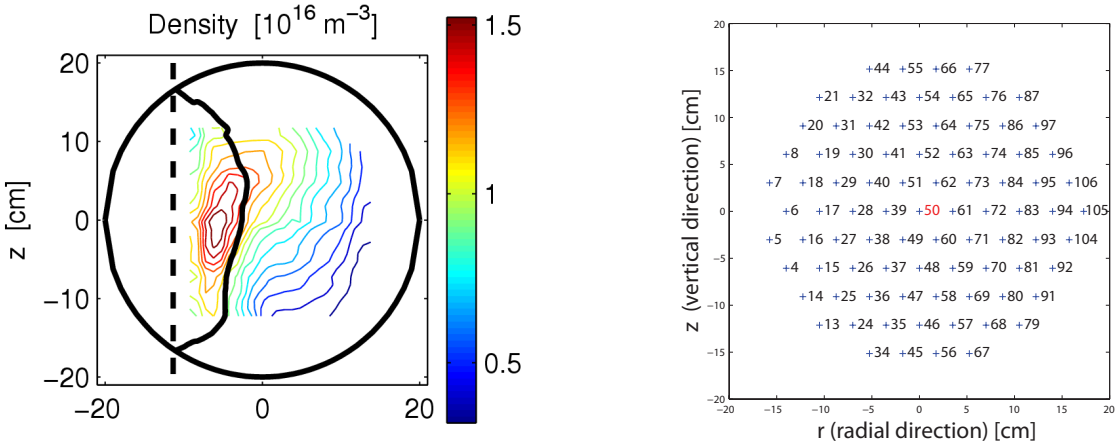

Figure 3.3: Left: A two dimensional plasma profile is shown together with the average location of the UH layer (solid line) and the position of the EC layer (dashed line). Right: The 86 tips of HEXTIP are shown with their number. r indicates the horizontal direction and z the vertical. Tip 50 lies at $r = z = 0$. LFS and HFS lie at $r > 0$ and $r < 0$, respectively.

In this work, I will analyze I_{sat} measurements, sampled at a rate of 250 kHz. In Fig. 3.4, the Langmuir probes installed on TORPEX are shown. HEXTIP [7] is a two-dimensional imaging probe. It covers the whole plasma cross-section with a resolution of 3.5 cm. SLP, TWEEDY and TRIP are movable probes. They can be shifted radially. SLP and TWEEDY can also be rotated around their axis. HEXTIP measures I_{sat} and V_{fl}, SLP, TWEEDY and TRIP can also operate with a swept voltage.

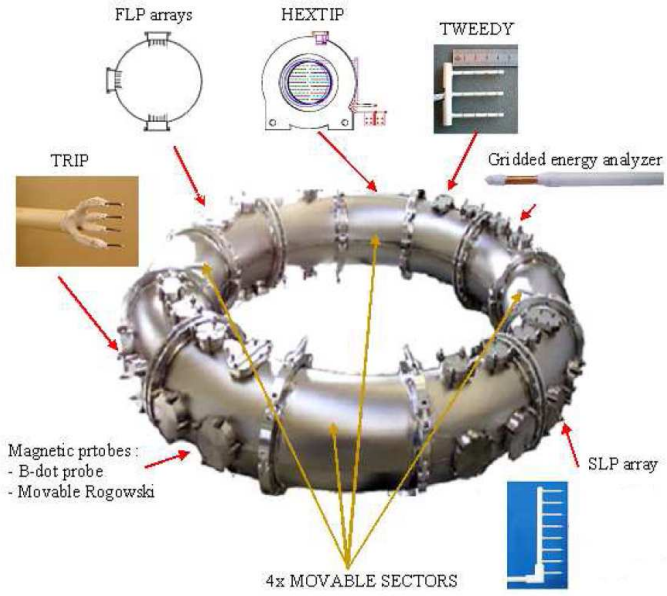

Figure 3.4: Scheme of TORPEX with its main Langmuir probes.

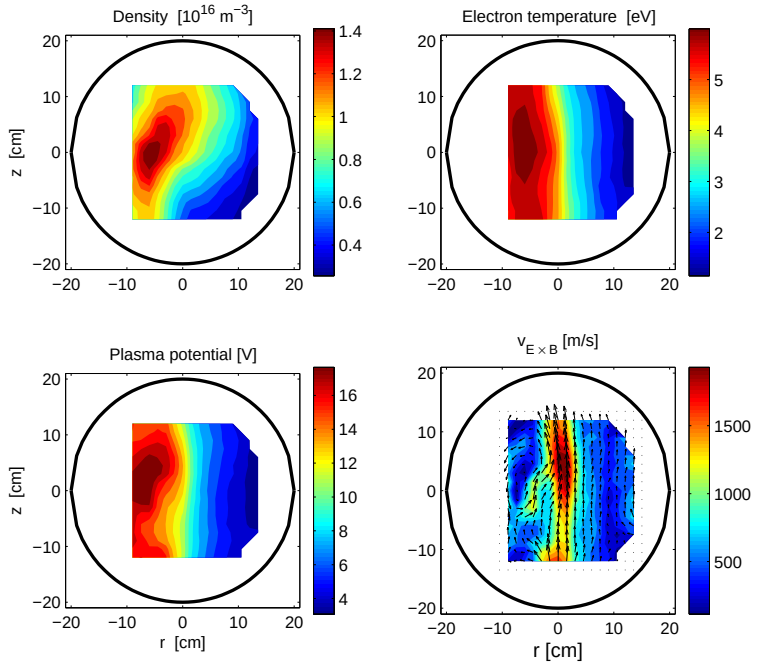

Figure 3.5: Two-dimensional, time-averaged profiles are shown. They are obtained with SLP by applying a swept voltage and reconstructing the I-V curve. SLP has been moved on a shot to shot bases to cover the main part of the cross-section.

3.2 Target plasma

Turbulent structures, or blobs, are observed in many different configurations in TORPEX [8]. In this work, a hydrogen plasma is studied which is sustained by a relatively low injected microwave power of 400 W. A toroidal field of 76 mT and a relatively high vertical field of 2.3 mT are applied. The neutral gas pressure is set to $\approx 3.5 \times 10^{-5}$ mbar. By the choice of a large B_z compared to the one yielding an optimal confinement and low microwave power, a rather slab like plasma is obtained, which is centered at the high field side (HFS).
Before the start of this diploma thesis, an experiment has been performed under this conditions using TRIP and TWEEDY as reference probes and SLP as the movable probe (see Fig. 3.4). TRIP was positioned at $r = z = 0$ cm, TWEEDY at $r = 13$ cm, $z = 0$ cm. Plasma discharges, in the following called shots, of 2.6 s were recorded for different positions of SLP, such that the main part of the cross-section was covered. TRIP and TWEEDY were measuring I_{sat} and SLP the current by applying a swept voltage. Using boxcar-averaging [12], the mean spatio-temporal evolution of n, T_e and V_{pl} was reconstructed by detecting a large number of blob events at TWEEDY. In the following, I will refer to this experiment as the $SLP\ experiment$. Mean profiles of density, electron temperature, plasma potential and $\mathbf{E} \times \mathbf{B}$ velocity are shown in Fig. 3.5. The CS-result from the $SLP\ experiment$ is shown in Fig. 3.6.

In this work, this plasma configuration is studied with data from HEXTIP. The disadvantage of this diagnostic compared to SLP is the poorer spatial resolution and the fact that it provides only I_{sat} and V_{fl}. An important advantage of HEXTIP is that the whole cross-section is covered at the same time, which allows to visualize directly the density fluctuations. This can help to interpret the results obtained with CS. In addition, HEXTIP allows to evaluate instantaneous

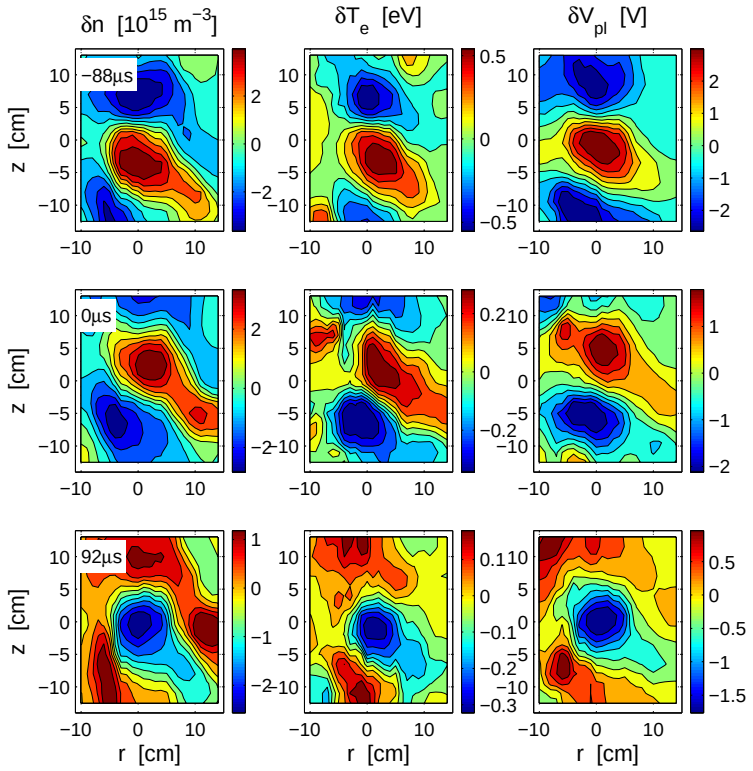

Figure 3.6: Shown are the CS-results for the fluctuating part of density, electron temperature and plasma potential. They are obtained from the SLP *experiment* with the reference probe in the blob region ($r = 13$ cm, $z = 0$ cm).

density gradients.
So, why use CS at all? First, the plasma is really quite turbulent and therefore, the average behavior leading to a blob might give more insights than a single event. Second, interesting CS-results from HEXTIP data can be verified in an SLP *experiment*, which yields more physical observables and a higher spatial resolution.
In Fig. 3.7 (a) and (b), the mean profiles of plasma density and floating potential obtained with HEXTIP are shown. Comparison with the density profile obtained from the I-V curve indicates an overestimation of around a factor 2. The floating potential profile strongly deviates from the profile of the plasma potential. The radial electric field derived from it would even give the wrong sign. Fourier spectra of I_{sat} measurements from HEXTIP indicate the presence of a dominant mode with a frequency of around 4 kHz in the laboratory frame (see Fig. 3.8 (a)). The skewness, i.e the third standardized momentum of the distribution function, also shows different characteristics in different poloidal regions, as is visible in Fig. 3.8 (b). In the HFS, the I_{sat} signals are positively skewed. This is expected for a region where fluctuations are mainly due to the passage of blobs. In the region of the mode, the skewness is close to zero. Negatively skewed signals are found for the positions of maximal mean density.
The CS-result from the SLP *experiment* in Fig. 3.6 shows a mode which is propagating upwards. A positive structure first starts to elongate and then gets sheared off to form a blob. The fact that SLP is toroidally separated from the reference probe in the blob region shows that the observed structures are toroidally elongated. The mode corresponds to the 4 kHz frequency-peak found in the power spectrum.

It is a general feature of TORPEX that the largest fluctuations are observed in regions where the pressure gradient is large and colinear to the magnetic field gradient [14]. The interchange mechanism plays an important role for the drive of the observed instabilities. It seems that the mode in this configuration is a pure interchange wave, in a nonlinear saturated stage. Within experimental uncertainty, there is no finite $k_{\|}$. The phase velocity $v_{ph} = -\frac{T_e}{eBR}$ which is expected for an interchange mode [3] or the electron diamagnetic drift characteristical for the phase velocity of drift waves, are both directed in the negative $z-$direction. The reason why the mode seems to propagate upwards is the $\mathbf{E} \times \mathbf{B}$ drift visible in Fig. 3.5.

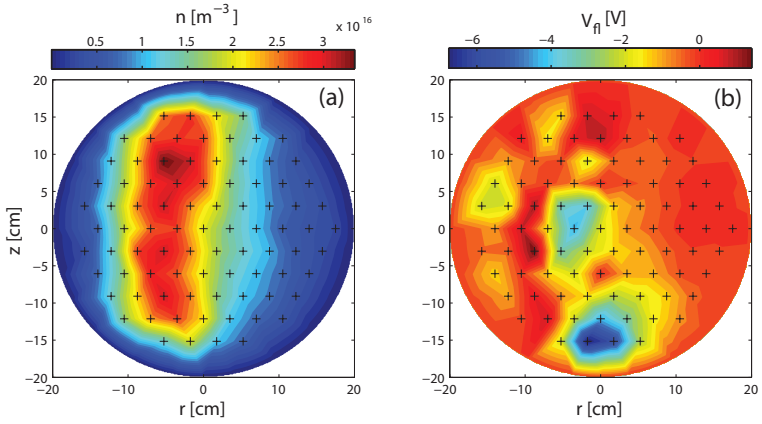

Figure 3.7: Profiles of mean density (a) and floating potential (b). The values measured at the 86 tips are linearly interpolated to give a two-dimensional profile.

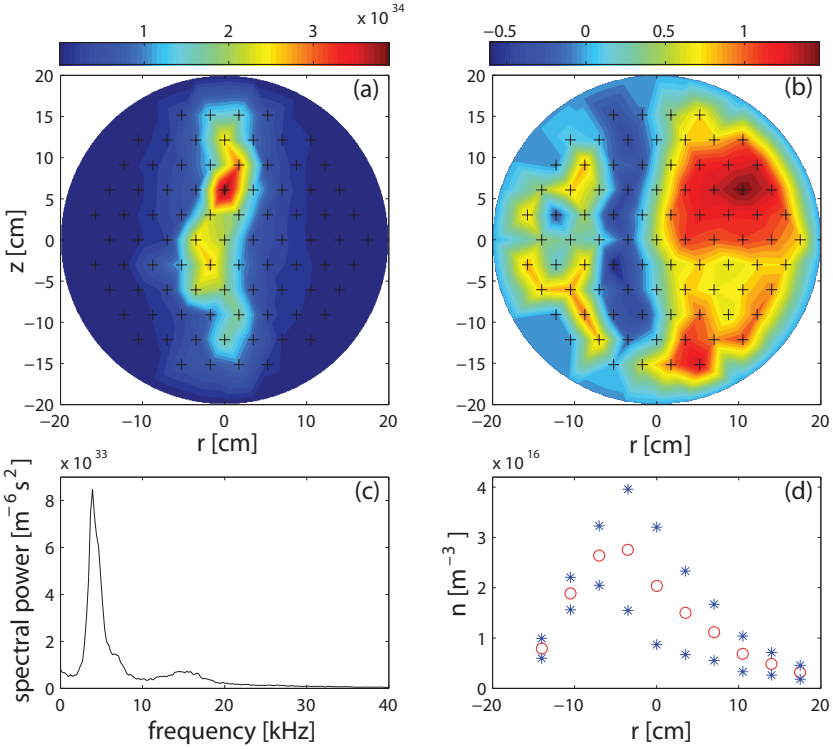

Figure 3.8: (a): Spectral power of $\tilde{n}$ in $\mathrm{m}^{-6}s$ between 3,2 and 4,8 kHz. (b): Skewness profile. (c): Power spectrum at HEXTIP-position 52. (d): Mean density profile at z=0 (circles) together with its standard deviation.

4

Experimental study of blob ejection in TORPEX

This chapter describes steps undertaken to investigate possible reasons of the blob ejection. First results from HEXTIP data and comparison with the $SLP\ experiment$ are shown in 4.1. The trigger condition is studied in 4.2. In 4.3, different locations of blob arrival not accessible in the $SLP\ experiment$ are investigated. An extensive study of a relation between blobs and density gradients is performed in section 4.4. This is done for blobs detected at two different vertical positions. In a first step, the gradients of interest are determined by triggering on the blob signal. In a second step, their role is studied by triggering directly on these gradients. In 4.5, the location of the source is experimentally determined for events that are likely to eject a blob.

4.1 First steps with real data and comparison with the $SLP\ experiment$

The crucial step in conditional sampling is the choice of a good trigger condition. In Fig. 4.1, sequences of the signal from TRIP and TWEEDY are shown. Theirs mean values have been subtracted, such that only the fluctuating part is shown.
TWEEDY is positioned in the blob region. In addition to a rather noisy background, there are intermittent bursty events. It seems therefore reasonable to choose the 'standard' trigger condition, namely a threshold. All local maxima that exceed a value of 3.9 times the standard deviation of the signal and which are spaced by more that $200\mu s$ are triggered.
Less obvious is the identification of a coherent structure for the signal from TRIP. The data

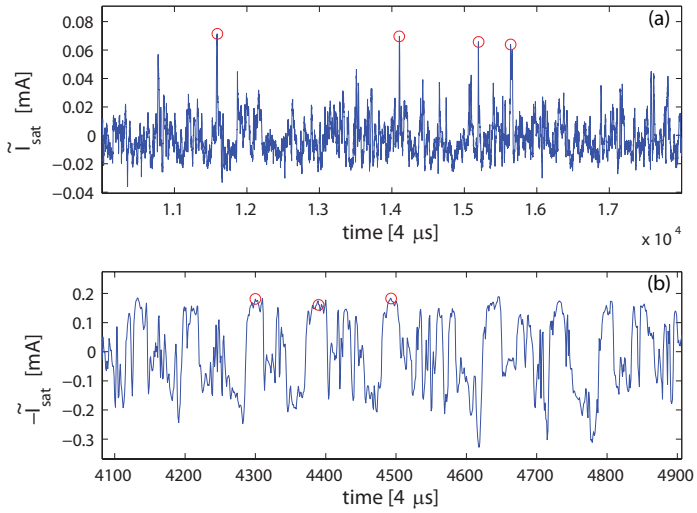

Figure 4.1: Figure (a) and (b) show part of the signals from TWEEDY and TRIP. The red circles indicate events that satisfy the trigger condition.

shows repeatedly occuring negative fluctuations of similar shape. Therefore, I took $-\tilde{I}_{sat}$ as the reference signal and triggered on events of a minimum width of $80\mu s$ at a hight of 0.1 mA.
The result obtained with data from HEXTIP is shown in FIG. 4.2. Column (a) and (b) show the result obtained by triggering on the TRIP and TWEEDY signal, respectively. For comparison, the evolution of a single event which caused a trigger at TWEEDY is shown in column (c). The mode is visible in all three cases. In agreement with the $SLP\ experiment$, the blob is observed in column (b) to originate from a positive wave crest. This wave crest elongated and gets sheared off. The blob is detected at TWEEDY at $\tau = 0\mu$s. Comparison between column (b) and (c) shows that individual events can deviate considerably from the average. HEXTIP and SLP are toroidally separated by $120°$. Therefore, a field line which intercepts the SLP-plane at a vertical position z will intercept the HEXTIP-plane at $z + \Delta z$, with $\Delta z = 1/3 \times 2\pi R\frac{B_\phi}{B_z} \approx 6.3$ cm. This is in agreement with the vertical separation of the blob in Fig. 3.6 and the one in the frame for $\tau = 0$ μs in column (b) of Fig. 4.2. Again an indication that the blob is field aligned. In addition, the vertical wavelength of the mode equals the gap between the first position a field line crosses the HEXTIP-plane and the second time after going once around the torus. The toroidal properties of the structures have been studied directly in an experiment, where SLP has been rotated around its axis by $15°$ from shot to shot, such that a circular area with radius ≈ 13 cm in the $toroidal$ direction has been covered. This has been done twice, once at a radial position of $r = -2$ cm and once at $r = 10$ cm. The CS-result shows toroidally elongated structures with no indication for an inhomogeneity along the field lines. A time frame of the CS-result is shown in FIG. 4.3.

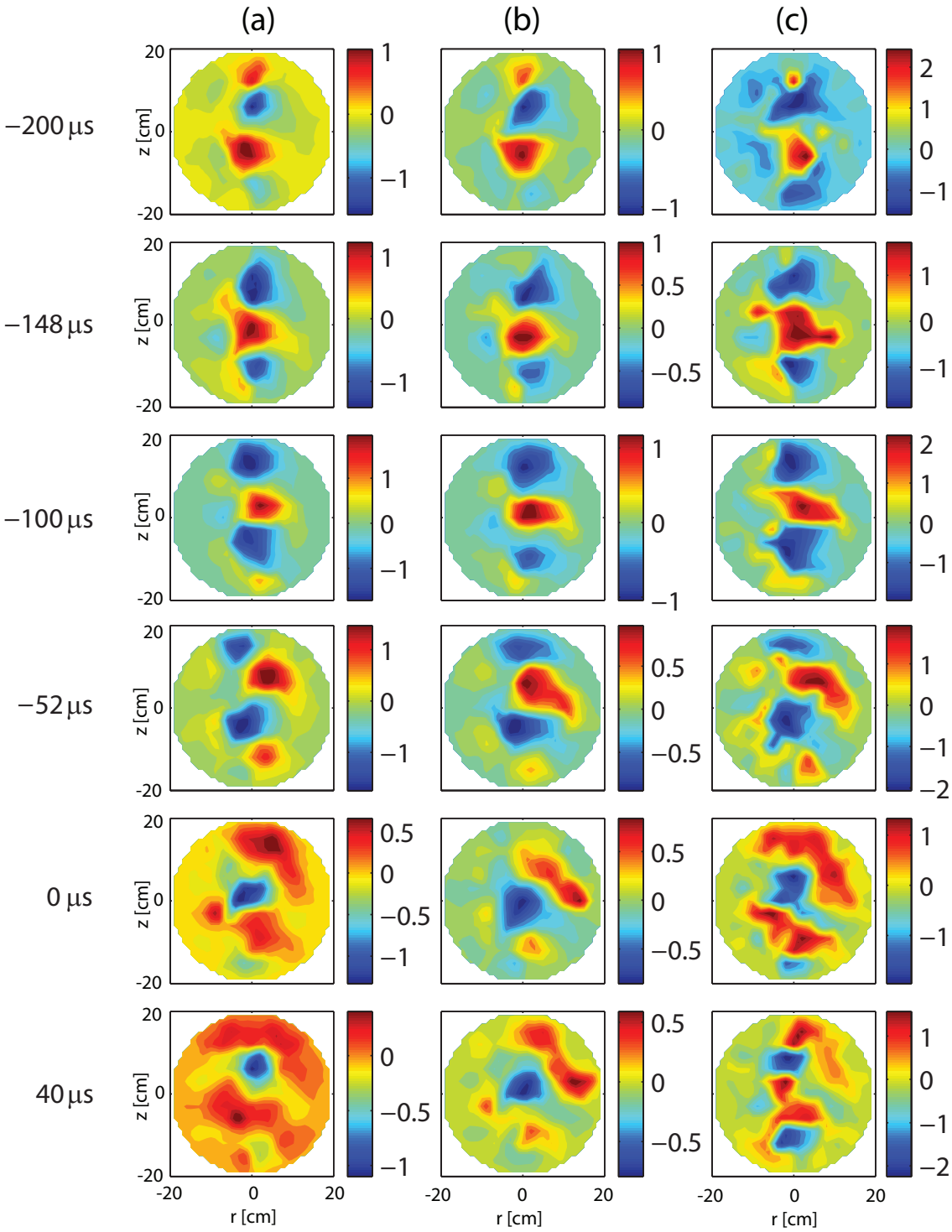

Figure 4.2: Shown are several frames of the evolution of $\tilde{n}$ (in 10^{16} m^{-3}), the fluctuating part of the density. Column (a) and (b) show the CS-result obtained by triggering on a signal in the mode region (TRIP) and in the blob region (TWEEDY), respectively. Column (c) shows the evolution of an individual event, which satisfied the trigger condition for TWEEDY. In the following, the radial and vertical axis will not always be labeled.

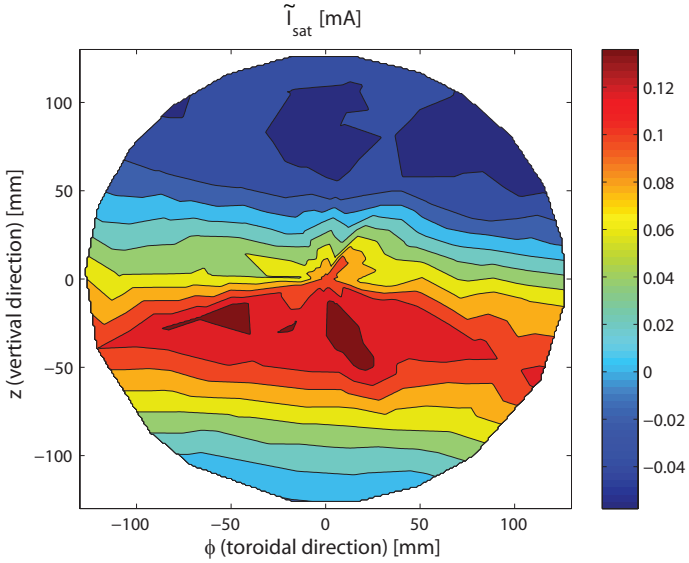

Figure 4.3: One frame of the toroidal profile of $\tilde{I}_{sat,cs}$ is shown. The reference probe was in the blob region. SLP was at $r = 10$ cm and has been rotated from shot to shot around its axis. The results for SLP at $r = -2$ cm and at $r = 10$ cm both show toroidally elongated structures moving upwards.

4.2 Study of the trigger condition

Conditional sampling gives the spatio-temporal evolution of an average coherent structure. This technique does not provide information on deviations of a single event from this average. In contrast to usual CS-experiments, HEXTIP allows to look at individual structures. But it is still useful to have a criterion which determines how similar the triggered events are. Such a criterion is given in [10]. There, a conditional reproducibility C^{rep} is defined by

$$C^{rep}(x,\tau) = \frac{\langle f \rangle^2_{ca}(x,\tau)}{\langle f^2 \rangle_{ca}(x,\tau)} \approx \frac{\left(\frac{1}{N}\sum_{i=1}^{N} f(x,t_i+\tau)\right)^2}{\frac{1}{N}\sum_{i=1}^{N} f^2(x,t_i+\tau)}, \qquad 0 \leq C^{rep} \leq 1 \tag{4.1}$$

$f(x,t)$ is the measured quantity, the t_i's are the times, when the trigger condition is satisfied and N is the total number of triggers. C^{rep} takes values between 0 and 1. It is small, when individual structures deviate strongly from the average and large, if they are very similar. A value of 0.5 is obtained, if the distribution of the values which contribute to the CS-result $f_{cs}(x,\tau)$ has a standard deviation equal to its mean value.
The reproducibility for the case, where the reference probe was in the blob region, is shown in Fig. 4.4. Reproducibility is observed to be rather high at maxima and minima of the mode, but low in between, where the amplitude is small.

C^{rep} can also serve as a tool to determine the effect of taking different or more restrictive trigger conditions. Let us illustrate this by looking at the TWEEDY-signal, shown in Fig. 4.1 (a). For a fixed threshold, instead of triggering on local maxima above this threshold, one could select events when the signal crosses the threshold value in a positive (or negative) slope. This showed nearly no effect, neither in the average nor in C^{rep}.

Reproducibility can certainly be enhanced by imposing a further selection among the events which satisfy a first trigger condition. As an example, the CS-signal at HEXTIP-position 50, which is obtained by triggering on the blob-signal, is shown in Fig. 4.5 (a). Also shown is the σ-band, introduced in section 2. From this, one expects that there are negative values at the time where the average takes its maximum. A histogram of the values which gave this maximum at around -112 μs is given in 4.5 (b). By selecting only the events which belong to counts in the histogram for values of $\tilde{n}$ above 0.5×10^{16} m^{-3}, C^{rep} can be enhanced considerably, without lowering much the total number of triggers. The effect is shown in Fig. 4.5 (c), where C^{rep} at HEXTIP-position 58 is plotted with and without this further selection.

So, C^{rep} can be enhanced by imposing more restrictive trigger conditions. However, one should still have enough triggers such that the CS-result has a statistical meaning. Although the number of triggers is usually not an issue at TORPEX, I want to give a rough idea of how many triggers are needed such that the CS-result is a reasonable estimate for the conditional average (see (2.1)). The conditional average is approximated by

$$\langle f \rangle_{ca}(x,\tau) \approx \frac{1}{N}\sum_{i=1}^{N} f(x, t_i + \tau). \tag{4.2}$$

Again, $f(x,t)$ is the measured quantity, t_i the times when the trigger condition is satisfied and N the number of triggers. The expectation value of the right side in (4.2) equals the left side. An idea of the accuracy of this approximation is obtained by looking at the standard deviation:

$$\begin{aligned}
\sigma^2 = \langle \big(\frac{1}{N}\sum_i f_i - f_{ca}\big)^2 \rangle &= \langle \frac{1}{N^2}\sum_{ij} f_i f_j - \frac{2}{N}\sum_i f_i f_{ca} + f_{ca}^2 \rangle \\
&= \langle \frac{1}{N^2}\big(\sum_i \big(f_i^2 + \sum_{i\neq j} f_i f_j\big)\big)\rangle - 2f_{ca}^2 + f_{ca}^2 \\
&= \frac{\langle f^2 \rangle_{ca}}{N} + \frac{N(N-1)}{N^2} f_{ca}^2 - f_{ca}^2 \\
&= \frac{\langle f^2 \rangle_{ca}}{N} - \frac{f_{ca}^2}{N} \\
&= \frac{\sigma_f^2}{N},
\end{aligned}$$

and therefore $\sigma = \frac{\sigma_f}{\sqrt{N}}$. Here, f_i stands for $f(x, t_i + \tau)$, f_{ca} for $\langle f \rangle_{ca}(x,\tau)$ and σ_f is the standard deviation of the random variable $(f(x, t+\tau)|C(f(x_{ref}, t))$. σ_f is usually comparable to the amplitude of the CS-result. This is directly visible in Fig. 4.5 (a), or indirectly in Fig. 4.4, where the reproducibility is around 0.5 in the mode region. In order to have a good estimate of $\langle f \rangle_{ca}$, σ should therefore be much smaller than σ_f. So, a number of at least 100 triggers is surely necessary.

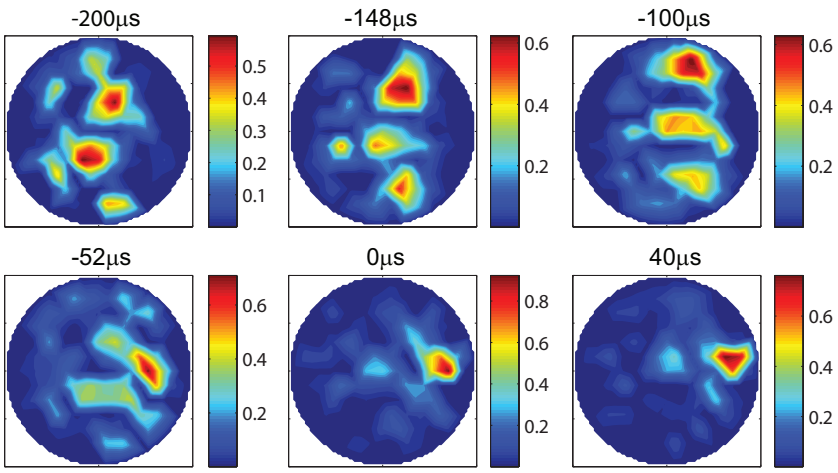

Figure 4.4: C^{rep} is shown for the CS-result of column (b) in Fig. 4.2.

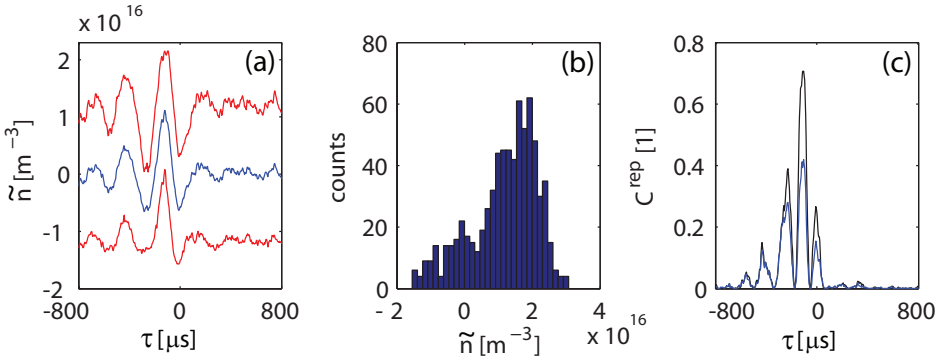

Figure 4.5: (a): CS-result at HEXTIP-position 50 (blue line) together with the σ-band. (b): Histogram of the values which gave the maximum amplitude in Fig. (a) at -112 μs. (c): C^{rep} at HEXTIP-position 58 with and without applying a further selection among the triggered events (black and blue line, respectively).

4.3 Blobs at different poloidal positions

In this section, I investigate blob events at different poloidal locations. So far, the reference probe was a tip from TWEEDY positioned at $r = 13$ cm, $z = 0$ cm. Since HEXTIP and TWEEDY are separated toroidally only by around $25°$ (see Fig. 3.4), this corresponds to about the same position in the HEXTIP plane. To see blobs at different vertical positions, I take now the points 91, 93, 95 and 97 from HEXTIP as reference probes. The locations of these tips are shown in Fig. 4.6. They lie at a radial position of $r = 12.25$ cm and are vertically distributed between $z = -9$ cm and 9 cm. A first thing to notice is that there really are blobs at all of these four positions. Fig. 4.6 shows the number of triggers as a function of the threshold level.
In section 4.1, we saw that the blob originates from a positive wave crest of a mode. Similar dynamics are found by using tips 95 and 97 as reference probes. For tip 93 and especially for tip 91 however, the CS-result looks quite different. A few time frames of the CS-result with x_{ref} at 91 are shown in Fig. 4.7, row (a). In the frame at 0μs, there are two blobs, one at the bottom and one at the top. The vertical distance between two points where a field line intercepts the HEXTIP plane is given by $2\pi R\frac{B_\phi}{B_z} \approx 19$ cm, which is consistent with the distance

of the two blobs. This shows again that blobs are field line elongated structures. A field line crossing the HEXTIP plane at $z = 0$ cm is already very close to the vacuum vessel when it comes back. Therefore we could only see one blob in section 4.1. More surprising is the fact that in the frame at -148μs, the plasma fluctuation looks much more slab like compared to the corresponding frame in Fig. 4.2, column (b), where the mode is clearly visible. One possible explanation for this observation is that there are two ways how blobs are generated: In some cases, they originate from a strong mode which suddenly elongates. But it also happens that the plasma is stable with no or only a small mode and at a given moment, the mode grows very fast and generates the blob directly. The reason why we see different pictures at different vertical positions could be due to a suppression of either of the two possibilities at a given vertical position. For example, it might be possible that a strong mode interacts with the vacuum vessel before it can give rise to a blob at tip 91, so that only the second possibility for blob generation is detected at this point. To check this hypotheses, I took a shot with SLP as reference probe. SLP was shifted and rotated such that one of its tips was at $r = 12$ cm and $z = -9.4$ cm, very close to the poloidal position of HEXTIP-tip 91, but toroidally separated by $120°$. By assuming perfect toroidal symmetry and homogeneity along the field lines, one would expect to see a similar picture at HEXTIP as by triggering on tip 91, only shifted by around $19/3$ cm ≈ 6.3 cm to the top. However, the CS-result visible in Fig. 4.7, row (b), shows a large positive wave crest already at $\tau = -148\mu$s. Possible explanations for this observation are that toroidal symmetry is disturbed by the effect of probes or by the localized position of the microwave source. Or there are really toroidal dynamics playing a role in the blob ejection. A further investigation of this is not possible at this point.
In the following, the two 'extreme' cases, i.e. blobs at tip 91 and 95, are further studied.

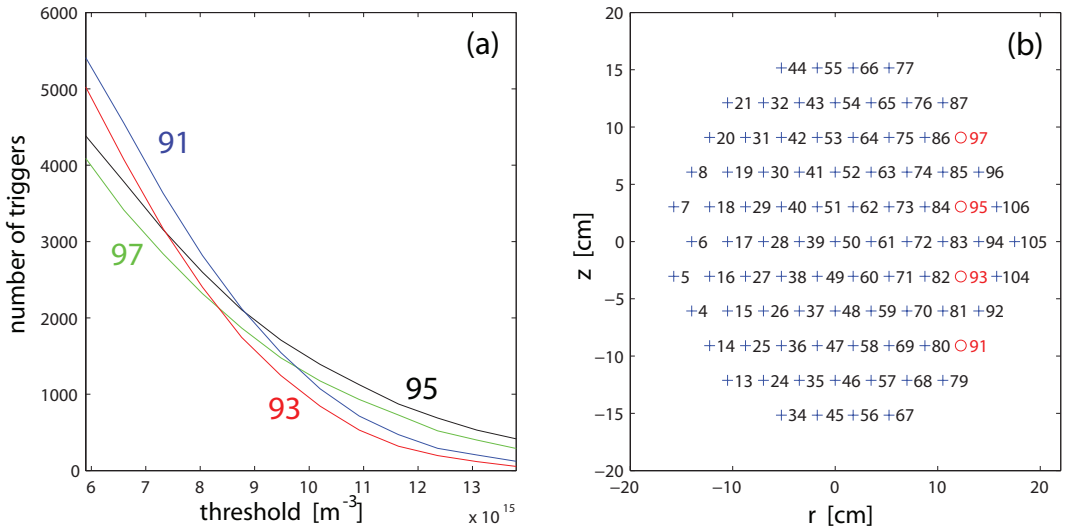

Figure 4.6: (a): The number of triggers is shown as a function of the threshold value for different tips as reference positions. A threshold value of 10^{16} m^{-3} means that only local maxima which exceed the mean value by this amount are triggered. The standard deviation of the reference signals are around 3×10^{15} m^{-3}.
(b): The number of the HEXTIP-tips are shown.

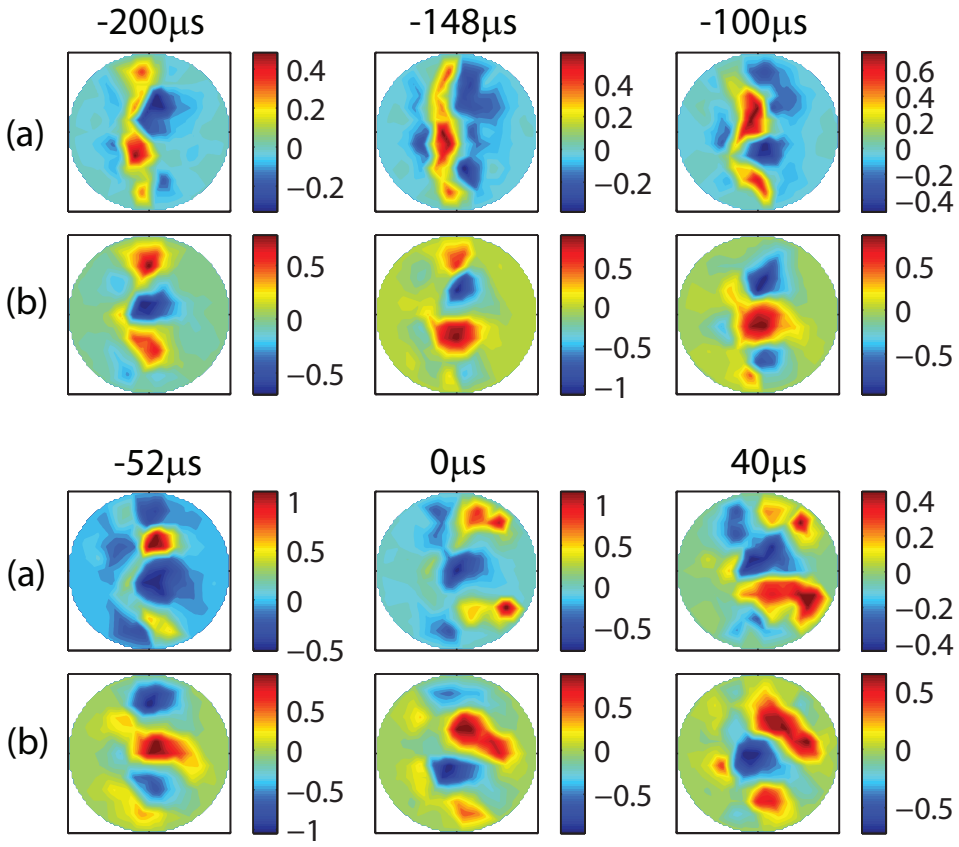

Figure 4.7: Shown is the CS-result of $\tilde{n}$ (in $10^{16}\mathrm{m}^{-3}$) in the HEXTIP plane. In case (a), the reference probe was tip 91. In case (b), the reference probe was a tip from SLP, positioned at a poloidal point close to the one of tip 91, but toroidally separated by $120°$.

4.4 Link between blobs and density gradients

The linear growth rate γ of the interchange instability in a curved magnetic field is given by

$$\gamma = \left[\frac{T_e + T_i}{m_i}\frac{2}{R} \quad |\frac{1}{n}\frac{dn}{dr}|\right]^{1/2} \propto |\frac{1}{n}\frac{dn}{dr}|^{1/2}, \tag{4.3}$$

for negative values of the normalized radial density gradient [3]. T_e and T_i are the electron and ion temperature, respectively, m_i is the ion mass, R the radius of curvature of the magnetic field. This result is derived from the linearized Vlasov equation in a simple slab geometry, neglecting temperature gradients and assuming a wavelength large compared to the ion Larmor radius. In this collisionless model, the interchange instability is unstable whenever there is a finite density gradient parallel to the magnetic field gradient. Effects such as for example diffusion due to collisions can stabilize the plasma up to a certain threshold value for the density gradient.
In [16], a computational approach is presented to study the nonlinear evolution of the interchange instability. Turbulent transport is found to be intermittent. Avalanche-like bursts are observed when the local radial density gradient exceeds the critical one. These theoretical and

numerical studies emphasis the possible role of the density gradient in triggering the blob events. In the following, I describe experimental steps undertaken to investigate the role of the gradient in the generation of blobs.

4.4.1 Trigger on the blob

The goal of this section is to identify the density gradients which might be responsible for the blob ejection and their relation to the size of the blob. Before focusing on blobs detected at tip 91 and 95, I describe here the applied techniques.

The normalized radial density gradient is approximated between two neighboring tips from HEXTIP by

$$\frac{1}{n}\frac{dn}{dr} \approx \left(\frac{n_R + n_L}{2}\right)^{-1} \times \frac{n_R - n_L}{\Delta r}, \tag{4.4}$$

where n_L and n_R are the instantaneous densities measured at the left and at the right tip and $\Delta r = 3.5$ cm is the distance between the two tips. Uncertainties due to a temperature gradient or electronic noise are neglected.
The reference probe is in the blob region (tip 91 or tip 95). The signal is searched for local maxima spaced by at least 200μs to ensure statistical independence. To detect blobs of different size, not the local maxima above a threshold are triggered, but the ones lying in the range between a lower and an upper bound (see Fig. 4.8). This is done for a succession of such 'trigger-windows'. The average gradient during these conditionally sampled time windows is evaluated for all gradients accessible in HEXTIP.
As it is pointed out in [2], a lot of care is required in the interpretation of amplitudes obtained with conditional sampling. On one side, there are error events, i.e. events that do not belong to any coherent structure, but are random fluctuations, which cause a trigger event. They can give rise to a strong loss in amplitude of the CS-result. On the other side, the coherent structure does not always evolve with exactly the same speed. This leads to a washing out of the CS-result.
More error events are to be expected for smaller trigger-windows than for higher ones. For the highest three trigger-windows, which are typically above 2.5 times the standard deviation of the reference signal, error events should be negligible. This is encouraged by Fig. 4.8, where triggered events from the third highest window are shown. To take into account the second point, I use a method in addition to the CS, which is less affected by a dispersion in time of the minima of the gradient. For every triggered event, time-windows of length $\Delta\tau$ centered around a time τ before the trigger are searched for the minimal value of the gradient. The mean value of the distribution of these minima is taken as the optimal value of the gradient at time τ. It is the value which would be found, if all the minima occurred exactly at the same instant. This is done for all trigger-windows and different values of τ.
It is important to keep an eye on the number of triggered events. For badly chosen trigger-windows with only a small number of triggered events, very misleading results can be obtained. Therefore, in the following, I will indicate the number of triggers found in every trigger-window.

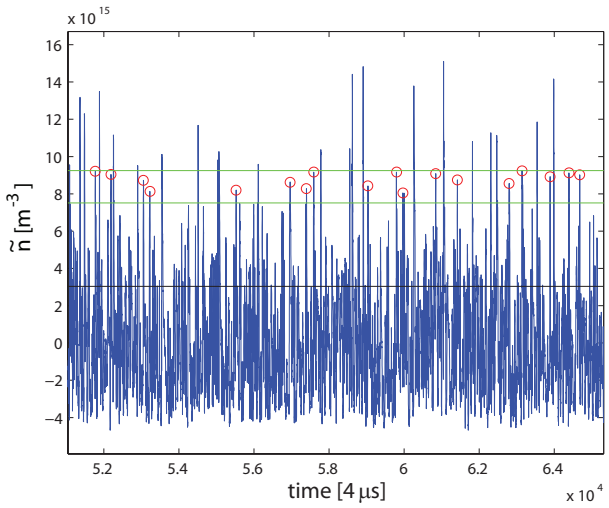

Figure 4.8: A sequence of the signal from tip 91 is shown. The red circles indicate the events found in the third highest trigger-window. The bounds of this window are indicated by green lines. The black line is at a hight of once the standard deviation of the signal.

Position 91

The reference signal is the fluctuating part $\tilde{n} = n - n_0$ of the density at HEXTIP-tip 91. Five trigger-windows are defined between 4.1×10^{15} m^{-3} and 11.6×10^{15} m^{-3}. In a sixth 'window', all local maxima above 11.6×10^{15} m^{-3} are taken. The number of triggers in the trigger-windows 1 till 6 are: 1075, 1428, 1777, 1644, 1106, 495, respectively.
To find the gradients which are possible candidates to trigger a blob event, I am looking for strong negative gradients before the growing of the instability. From the CS-result, the instability seems to start growing at around -160μs with respect to the time of the arrival of the blob at the reference probe. The CS-result of the gradients at that instant, obtained with triggers from the highest trigger-window, is shown in Fig. 4.9. The absolute value of each gradient is shown as well as the fluctuating part, i. e. the gradient minus its mean value. For convenience, the density gradient between two tips is taken as the gradient at the left tip. Negative gradients over a band between $r = -3.5$ cm and $r = 0$ cm are visible. The smallest gradients are found at tips 46, 47 and 45. In Fig. 4.10 (a), the time evolution of the CS-result of the gradient at tip 47 is shown for different trigger-windows. Fig. 4.10 (b) shows the mean value of the distribution of minimal gradients for different τ. The value of $\Delta\tau$ was set to 120 μs, which is roughly the width of the negative peaks of the gradients in figure (a).
The same trend is visible in both figures, which implies that larger gradients belong to larger blobs. This is already the case for the three highest trigger-windows, where error events should be negligible. The instant of negative gradients also seems to move slightly back in time for lower trigger-windows, indicating that dynamics leading to larger blobs evolve faster.

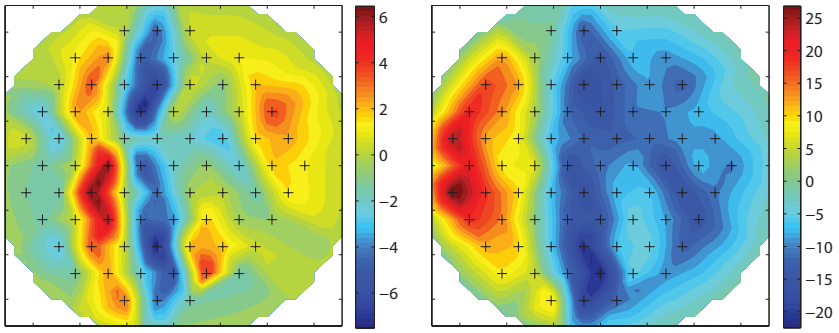

Figure 4.9: CS-result of the fluctuating part of the normalized gradient (left) and its total value (right) in m^{-1} and at $\tau = -160$ μs. The reference position for the CS was tip 91.

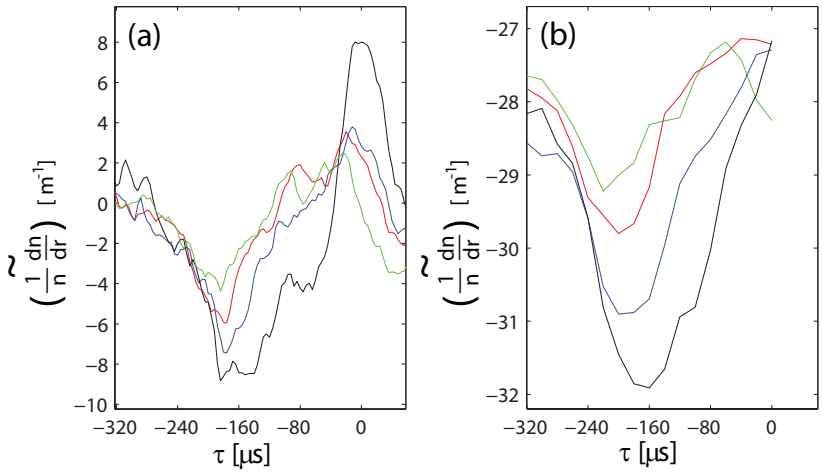

Figure 4.10: (a): CS-result of the gradient at tip 47 for trigger-window six (black), five (blue), four (red) and two (green). Note that the fluctuating part of the gradient is shown, meaning that its mean value has been subtracted. (b): For the different trigger-windows and different values of τ, the mean value of the distribution of minimal gradients in the time-window of length $\Delta\tau$ around time τ is plotted, again for tip 47 (same colors as in (a)).

Position 95

The same is done now for blobs detected at tip 95. Five trigger-windows are defined between 3.9×10^{15} m^{-3} and 14.2×10^{15} m^{-3} and a sixth for the values above 14.2×10^{15} m^{-3}. The number of triggers in the trigger-windows 1 till 6 are: 1124, 1365, 1498, 1307, 853, 452, respectively. From the CS-result, the positive wave crest seems to start elongating at -80 μs. The CS-result of the gradients at that instant, obtained with triggers from the highest trigger-window, is shown in Fig. 4.11. The smallest gradients are found at tips 35,36 and 42. Again, the time trace of the gradient and the mean value of the distribution of minima for different values of τ is shown in Fig. 4.12 (a) and (b), for tip 35. A similar trend as in the last paragraph is visible. However, the monotonic decrease of amplitude of the gradient in (a) is not totally recovered in (b).

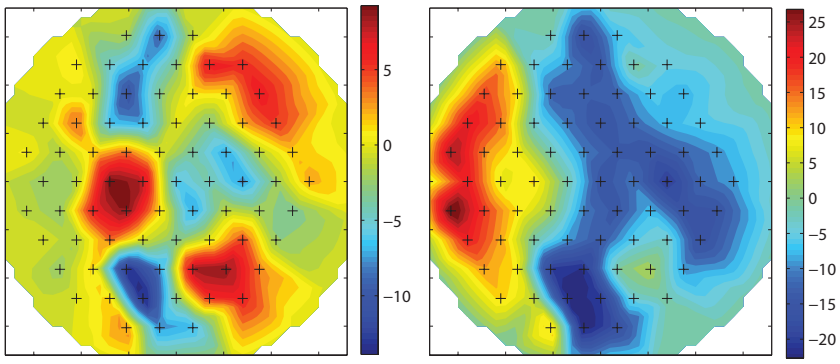

Figure 4.11: CS-result of the fluctuating part of the normalized gradient (left) and its total value (right) in m^{-1} and at $\tau = -80$ μs. The reference position for the CS was tip 95.

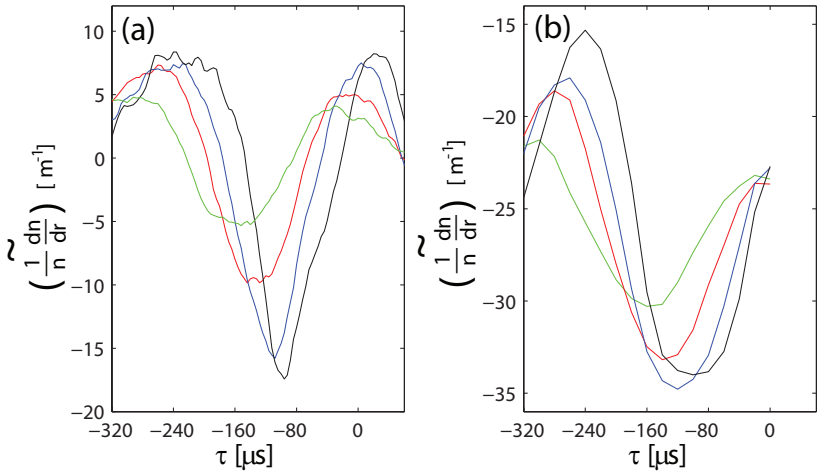

Figure 4.12: The same is shown as in Fig. 4.10, but for the gradient at tip 35 and blobs detected at tip 95. The colors black, blue, red and green correspond again to trigger-window six, five, four and two.

The location of the strongest gradients before the blob ejection has been determined from the CS-result obtained with triggers from the highest trigger-window. Using the CS-result obtained from blobs of different size could a priori give another result. However, this turned out not the be case.

4.4.2 Trigger on the gradient

In the preceding section, the positions of the gradients which might be responsible for the blob ejection were determined. In this section, I want to investigate the role of the density gradients in the blob ejection mechanism by triggering directly on these gradients. The goal is to see, if there is any indication for a critical gradient. A possibility would be to look at the amplitude of the CS-result obtained from this for signals in the blob region. But since blobs give rather narrow peaks in these signals, this amplitude is strongly affected by a dispersion in the blob

arrival time. I will therefore use another approach. For every triggered event and different instants τ after these events, the maximal value within a window of length $\Delta\tau$ around τ is stored. The same is done for a random trigger, i.e. a trigger that randomly selects events in the reference signal. All maxima above a certain threshold are interpreted as blobs. Finally, a two-dimensional plot is generated, which shows the number of blobs found with the 'physical' trigger condition divided by the number of blobs from the random trigger, and this for different instants and different blob-thresholds. This gives an approximation of how more likely it is to find a blob after the detection of a strong gradient, than it is by just guessing. In the following, I will refer to this plot as the *probability chart*.
A parameter to chose is the size $\Delta\tau$ of the window which is scanned for the maximum in the blob-signal. On one side, this window should be narrow enough to be characteristic for the time τ around which it is centered. On the other side, it should be large enough to allow for different arrival times of the blobs. In addition, I want that for most triggers, the detected maximum is really a local peak, i.e. a blob, and not an extremum at the border of the interval. The frequentness of the maxima at the border of the time interval is plotted in Fig. 4.13 (a) as a function of the window length. In the following, a window length of $80\ \mu$s is used. The fraction of the number of blobs from the 'physical' trigger and the number from the random trigger is subject to statistical fluctuations. The fluctuations coming from the random trigger can be controlled by taking a very large number of triggered events, and normalizing afterwards the obtained distribution of maxima to the number of events from the 'physical' trigger. To get an idea of the fluctuations, the *probability chart* is shown in Fig. 4.13 (c), for the case where the 'physical' trigger is a random trigger as well. The number of triggered events is set to a typical value of around 4000. Only the values are shown, where both numerator and denominator are larger then 10.

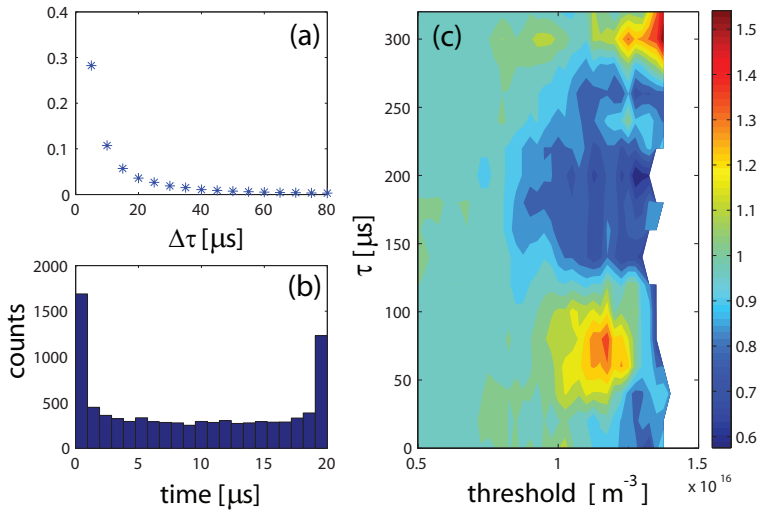

Figure 4.13: (a): The frequentness of the maxima found at the border of the interval is plotted as a function of the window size $\Delta\tau$. A random trigger was used. (b): Shown is a histogram of the position in the time window where the maximal value in the blob signal was found, for the chosen value of $\Delta\tau$. (c): The *probability chart* is shown for the case where the 'physical' trigger was a random trigger. τ indicates the time after the triggered events. The threshold is the value above which a local peak in the blob signal is interpreted as a blob.

Position 91

In section 4.4.1, we saw that at the time when the blob ejection starts, there are negative gradients between $r = -3.5$ cm and $r = 0$ cm. The smallest gradients were found at tips 46, 47 and 45.
The *probability chart* for tip 91 obtained by triggering on the gradient at tip 47 and for different trigger-windows is shown in Fig. 4.14. Three trigger-windows were defined, one for gradients smaller than -49.5 m^{-1}, one for gradients between -49.5 m^{-1} and -46.5 m^{-1} and one for gradients between -46.5 m^{-1} and -40 m^{-1}. These are the total values for the gradients. To compare them with the ones in Fig. 4.10 (b), the mean value of -14.7 m^{-1} needs to be subtracted. The number of triggers found in the three trigger-windows are 3517, 4586 and 3055, respectively.
The *probability chart* from trigger-window one, i.e. the trigger-window with the strongest gradients, shows a probability up to around 2.5 times higher to detect a blob than with a random trigger. The time of maximal probability is in agreement with the expected 160μs from section 4.4.1. For trigger-window two, a quite similar picture is obtained. However, values of around 2.5 are only achieved for large thresholds, where the uncertainty of the result is large. A completely different picture is visible for trigger-window three. There, no values above 1 are obtained. We have found the same trend as in the opposite case, where the trigger condition was on the blob signal from tip 91.

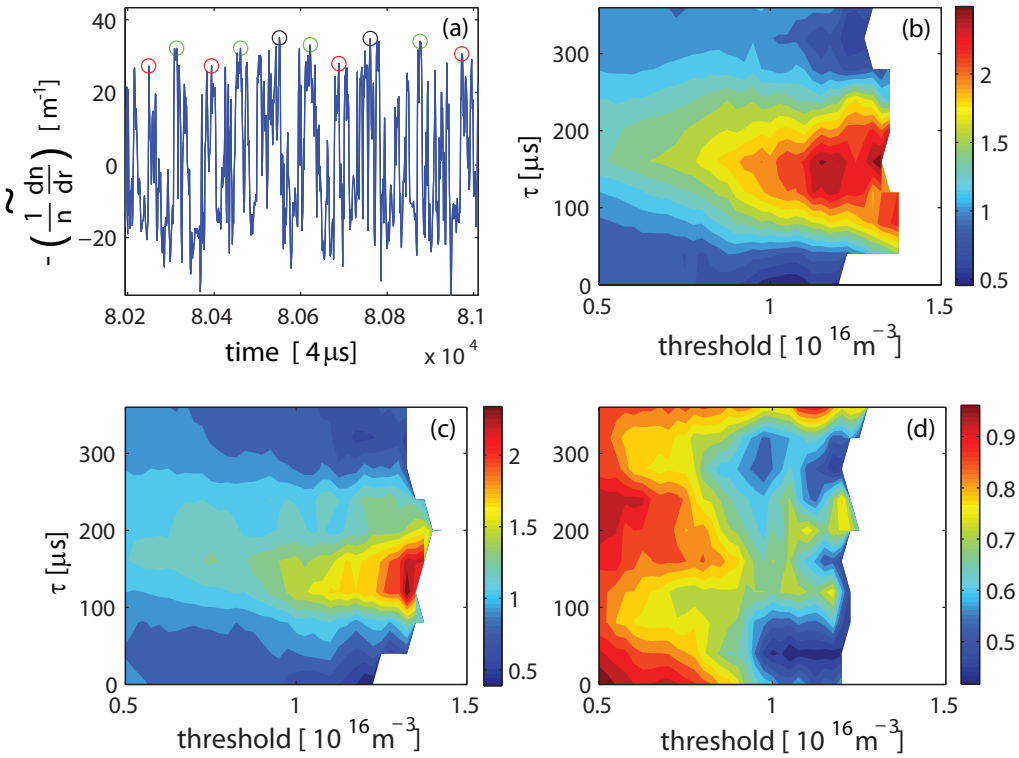

Figure 4.14: In (a), a sequence of $-n^{-1} \times dn/dr$ is shown. Triggered events are indicated with circles for trigger-window one (black), two (green) and three (red). In (b)-(d), the *probability charts* for trigger-windows one till three are shown.

In addition to this purely local detection of the gradient, I want to use a more global approach now. I select slab like profiles in the data and study the effect of the gradient only in these cases. To find such initial configurations, a routine is used which calculates the spatial Fourier transform for HEXTIP-data.
The profile of the CS-result at $\tau = -160\mu$s, obtained from triggering on blobs at tip 91, as well as the absolute value of its Fourier transform is shown in Fig. 4.15, column (a). Two peaks in the Fourier spectrum are visible for $k_r \approx \pm 45$ m^{-1} and $k_z = 0$ m^{-1}. In a first attempt to find slab like plasma configurations, I took this Fourier component as the reference signal and searched it for local maxima which exceed a threshold. The conditionally averaged profile at the instant of the trigger-events is shown in row (b). The radial 'mode' does not have the right phase and there is also a strong vertical $k-$component. Only by imposing another constraint, namely a small absolute value for this vertical $k-$component, a slab like profile is found (see row (c)). This second constraint has decreased the total number of tiggers from 4851 to 1076. The $probability\ chart$ for these events is shown in Fig. 4.16 (a). A strongly enhanced probability for blobs at tip 91 is visible for times of around the expected 160μs.
In a next step, two groups are formed from these 1076 events. The first group consists of events with a gradient at tip 47 between -48 m^{-1} and -40 m^{-1}, the second group of events with gradients below -48 m^{-1}. The minimal gradient does not need to coincide with the time of the trigger. Therefore, the minimal value in a time window of 80 μs around the instant of the trigger has been taken for the gradient.
To compare the two groups, the mean value of the distribution of maxima found after each trigger in a window $\Delta\tau = 80$ μs centered around τ is plotted for both groups in Fig. 4.16 as a function of τ. For $\tau = 160$ μs, the mean value of the group with stronger gradients is 15% larger than the one for weaker gradients.

This shows that a slab like configuration, where not the gradient at a single point, but the vertically averaged gradient is enhanced, has a rather high probability to generate a blob. This probability is increased by taking a subset of events with a strong gradient at a single point.

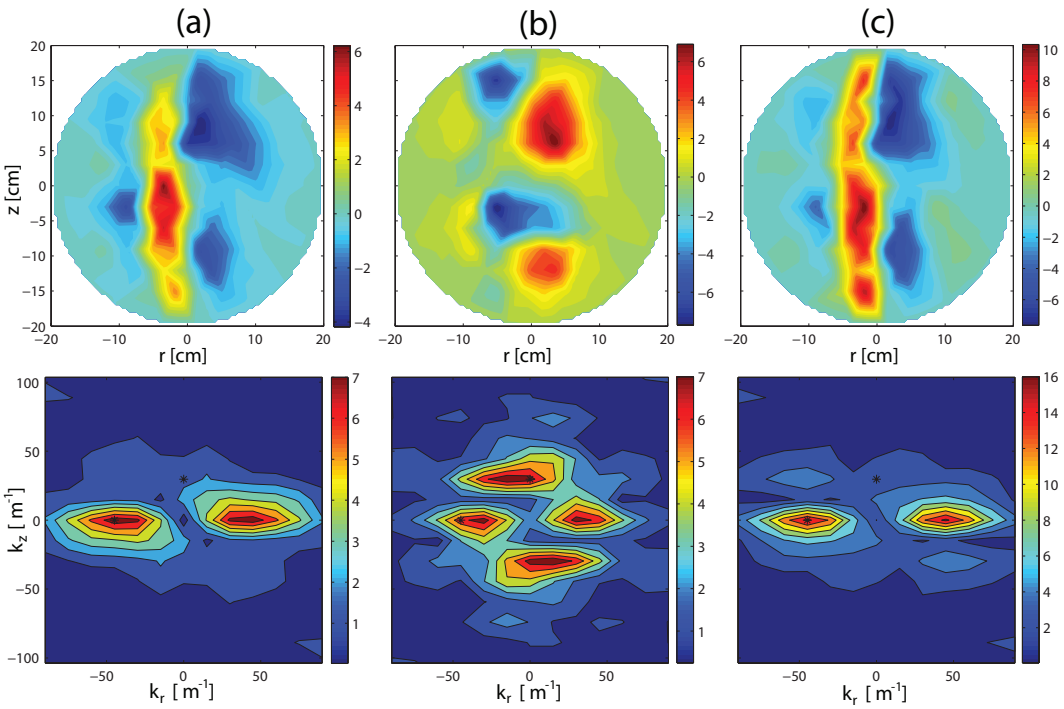

Figure 4.15: In the top row $\tilde{n}_{cs}$ in 10^{15} m^{-3} is shown, in the bottom row its Fourier transform in arbitrary units. Column (a): CS-result at $\tau = -160$ μs, obtained from triggering on tip 91. Column (b): CS-result at $\tau = 0$ μs, where the trigger condition was a large radial $k-$component. Column (c): CS-result at $\tau = 0$ μs. The trigger condition was a large radial as well as a small vertical $k-$component.

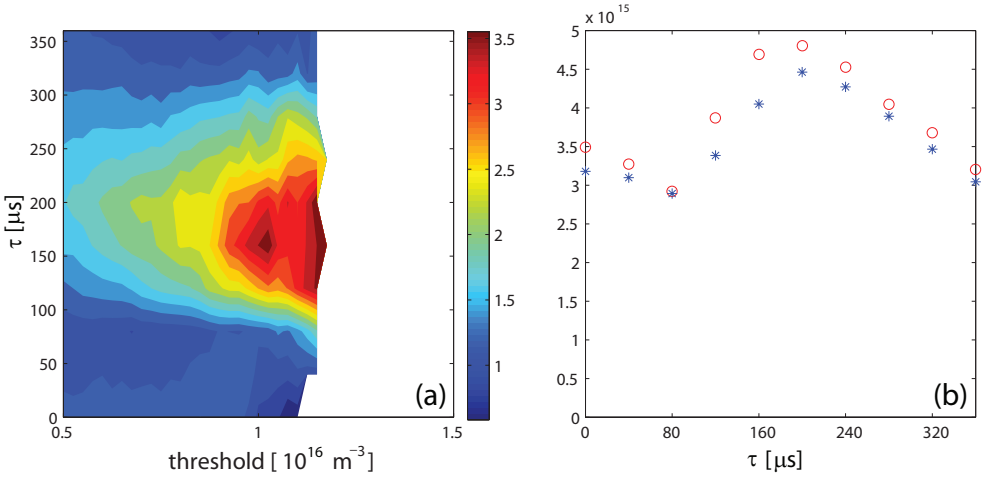

Figure 4.16: (a): The *probability chart* is shown for the 1076 events with a large radial and a small vertical $k-$component. (b): The mean value of the distribution of maxima is shown for the group of weak gradients (blue stars) and the one of strong gradients (red circles).

Position 95

Now, I focus on the gradient at tip 35 and its relation to blobs at tip 95. Four trigger-windows are defined for gradients below -47 m^{-1}, and gradients between -47 m^{-1} and -43 m^{-1}, -43 m^{-1} and -38 m^{-1} and -38 m^{-1} and -30 m^{-1}. The number of triggers are 4569, 4222, 2260 and 844, respectively. The obtained *probability chart* in Fig. 4.17 shows an enhanced probability of blob detection at around the expected 80 μs. A clear difference is only visible for the forth trigger-window, where the number of triggers is small.
To confirm this result, I repeat the same analysis, but with data from another session, where longer time series are available. The control parameters were very similar with a slightly enhanced natural gas pressure. The measured mean density profile is shifted a little towards the LFS. The same procedure as in section 4.4.1 shows that the strongest negative gradient before the elongation of the mode is located now at tip 47. Nine trigger-windows for gradients between -54 m^{-1} and -34 m^{-1} are chosen. All the windows contain at least 1500 events. The *probability chart* as well as the CS-result at the instant of the trigger is shown in Fig. 4.18, for trigger-window one, three, five, seven and nine. It is the result of 22 identical shots. A monotonic relation between the amplitude of the gradient and the probability to detect a blob is found. This relation is visualized in another way in Fig. 4.19. The probability to detect a blob after a gradient of a certain hight is shown, for different thresholds above which a value is interpreted as a blob. This probability is estimated in the following way. For every trigger-window, the number of values in the distribution of maxima which exceed a threshold is evaluated. Then, this number is divided by the number of total counts in this distribution. Since the peaks in the *probability charts* are located at different values of τ for different trigger-windows, the value of τ is chosen which gives the highest probability in each case.

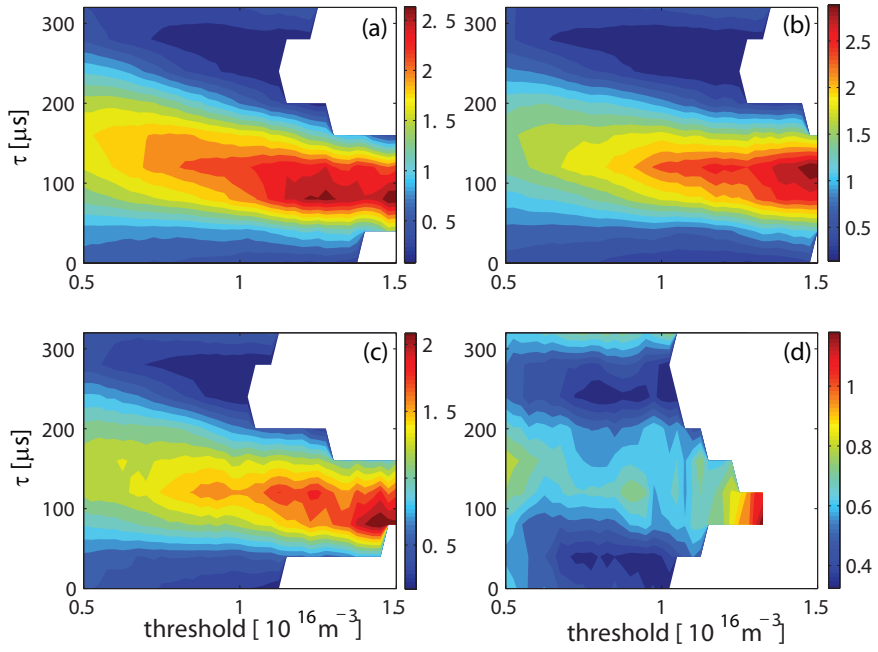

Figure 4.17: (a)-(d) show the *probability charts* for blobs at tip 95 and trigger-windows one till four.

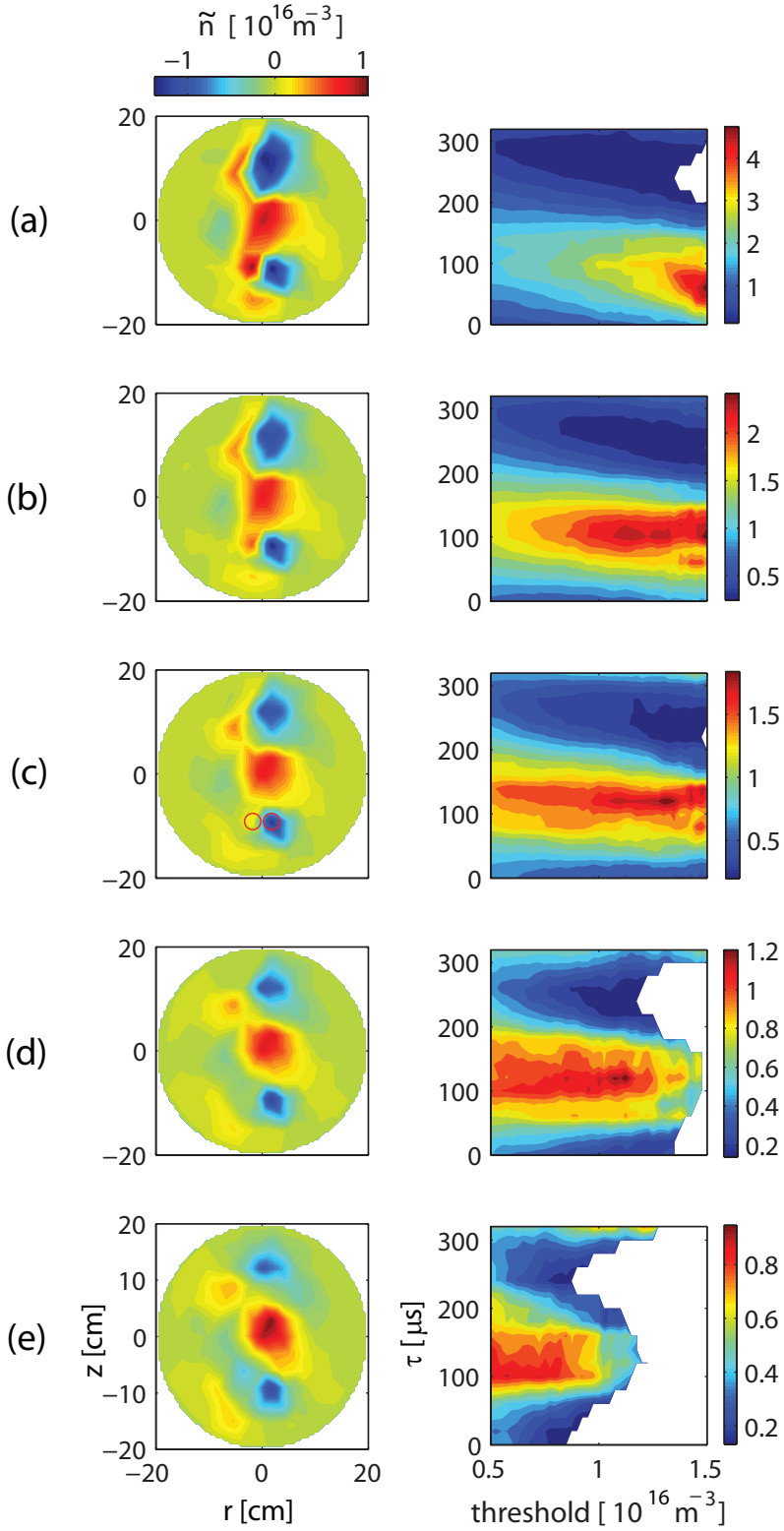

Figure 4.18: (a)-(e) shows the CS-result at the instant of the trigger as well as the *probability chart* for gradients in the trigger-windows one, three, five, seven and nine. The frame in (c) shows the location of tip 47 and 58, where the gradient has been measured.

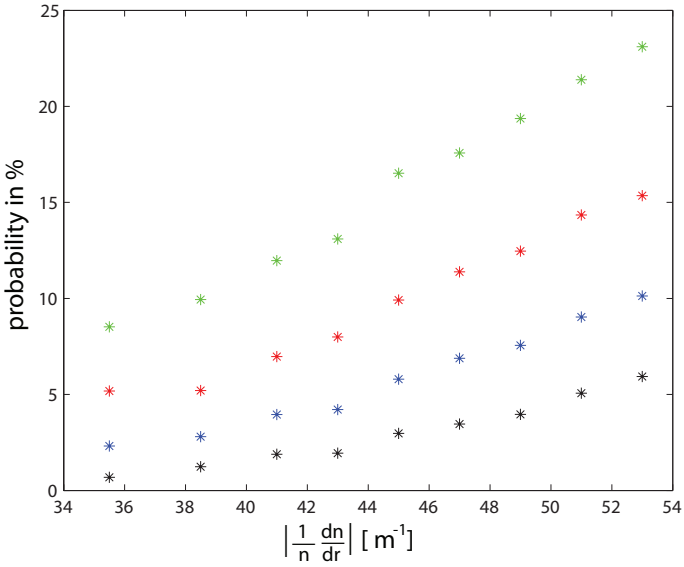

Figure 4.19: The probability to detect a blob is plotted as a function of the gradient. This is done for different blob-thresholds. The black points correspond to a threshold of 1.2×10^{16} m^{-3}, the blue, red and green points to one of 1.0×10^{16} m^{-3} , 0.8×10^{16} m^{-3} and 0.6×10^{16} m^{-3}, respectively.

This result shows similarities with the dynamics of avalanche-like burst found in the computing model in [16]. There, poloidal structures of the electric potential are observed, which generate regions with inward and outward fluxes. In the inward flux regions, matter is convected from the wall (LFS) into the core, which opposes the driving outflux. The accumulated matter stiffens the radial density gradient. Once the local slope exceeds the critical one, the system becomes unstable and generates an outward avalanche. We know from the SLP *experiment* (Fig. 3.6), that there are such poloidal structures of electric potential in our case. There is a phase shift between density and potential fluctuations, such that a local inward flux is to be expected in the region of negative wave crests.
It should be noted that the local radial normalized density gradient in [16] is not the one at a single position, but the value averaged along the vertical direction.
In our case, it is only the gradient between tips 47 and 58 that has been considered. However, the CS-result in the first column of Fig. 4.18 implies that it is not only the local gradient which changes from window to window, but the averaged gradient along the vertical direction as well. The negative wave crest at tip 58 has about the same amplitude in all cases. It is the value at tip 47 that changes. And this value extends along the vertical direction.
It is difficult to say from Fig. 4.19 if there is a critical gradient or not. A trend is clearly visible, but there is no evident transition between gradients which lead to a blob and gradients which do not. The question is, if we could expect a clearer result from this analysis. We should keep in mind that the gradient was detected between two tips only. We can not expect that the maximal gradient is always captured in this way. Sometimes, the profile might be shifted a little and we detect a weak gradient even though it is actually a strong one, which gives rise to a blob. In addition, the determination of the gradients is affected by uncertainties in the measured density.

4.5 Modulation of the source

So far, the particle source has not been considered at all in the dynamics leading to blobs. We know from [13] that the main plasma source lies at the UH layer, i.e at positions where the plasma density satisfies

$$n_{\mathrm{UH}} = \frac{m_e \epsilon_0}{e^2}\left(\omega_{rf}^2 - \frac{e^2 B^2}{m_e^2}\right). \tag{4.5}$$

For small values of n, the source lies close to the EC layer in the low field side. For large values of n however, it can move far into the high field side.
To have a first idea of the location of the source in an instantaneous profile, I evaluated its position with Eq. (4.5) and the measured density from HEXTIP. This location depends strongly on the accuracy of the measurement. This is illustrated in Fig. 4.20, where the UH layer is shown for the measured density as well as for half of its value. If it is true that the UH layer is so strongly deformed by the mode as seen in Fig. 4.20, another reason for the formation of blobs might need to be considered. Maybe, when the mode reaches a certain amplitude, a positive wave crest is amplified directly by the source and a new instability grows on top of it and results in a blob, independent of the dynamics to the left of the mode.
To determine experimentally the location of the source, I use a method similar to the one in [13]. The injected microwave source is modulated by square pulses of increased power and the behavior of the plasma is studied in the presence of such pulses as well as during times clearly separated from them. To see the effect of the pulse on a strong mode, an appropriate trigger condition is required to detect such structures. From the triggered events, a first group is formed with events were there was no micro-pulse close to that instant. A second group consists of the events where the pulse falls (by chance) in a desired time window after the triggered event. Finally, the two CS-results obtained from this are compared. The difference of the two should show the average location of the source for the detected structure, besides random fluctuations due to a limited number of triggered events.

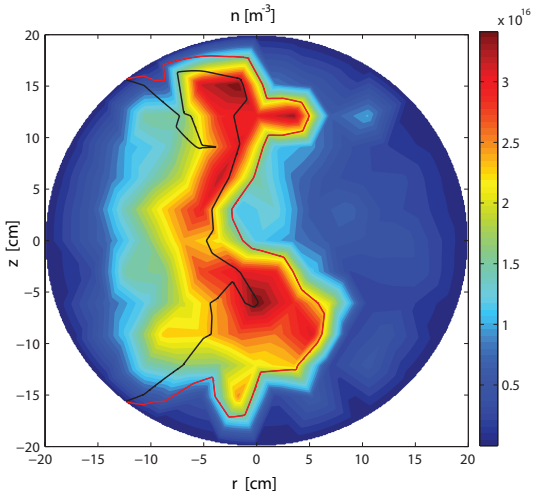

Figure 4.20: An instantaneous plasma profile is shown. The position of the UH layer is calculated for the measured density (red line) as well as for the density divided by two (black line).

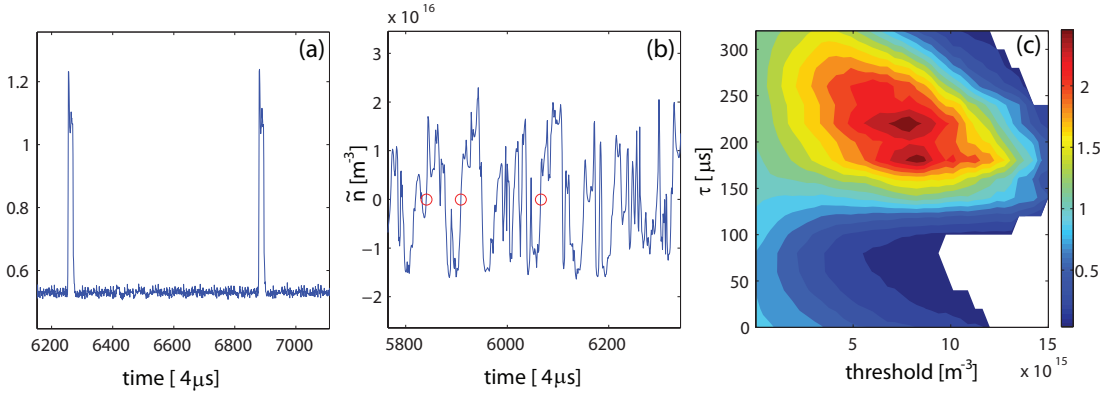

Figure 4.21: (a): A sequence of the injected microwave power is shown (in arbitrary units). (b): Three triggered events in the signal from tip 48 are shown. (c): The $probability\ chart$ for the triggered events without a micro pulse is given.

The experiment is performed with the same external control parameter as before, except the pulses of 1.5 kW and duration 75 μs. They occur with a frequency of 400 Hz, so at around every tenth cycle of the mode. Part of the signal of the ejected microwave power is shown in Fig. 4.21 (a). Tip 48 is used as the reference probe. Events are triggered where the signal exceeds the mean density for at least 80μs and achieves a value of $1.5 \times 10^{16}\mathrm{m}^{-1}$ during that time. The idea is to detect rather large positive wave crests. Events which satisfy this trigger condition are shown in Fig. 4.21 (b). 6438 events are found with no micro pulse in a time window between -720μs and 400μs around the trigger. The $probability\ chart$ is given in (c). We see an enhanced probability for blob detection at a time of around 200μs. Now, events are selected with a pulse starting to act between 104μs and 120μs. This is around the time, when a possible elongation of the mode starts. Note that the pulses which fall in this time window have no effect on the first trigger condition. 116 such events have been found. In Fig. 4.22, the CS-result for the triggers without micro-pulses as well as the difference between the result with and without pulses is shown for three instants. The effect of the source is clearly visible already for a short action of the pulse. In the first frame, we see a rather narrow band to the left of the mode, which is vertically elongated. It is only slightly deformed by the positive wave crest. In the next two frames, the difference in density achieves already a very high level and the plasma is strongly deformed by the pulse. The original position of the source might therefore have changed. These observations suggest that the source stays to the left of the mode, even if the amplitude of the latter is relatively large. The source steeps up the radial gradient in a rather uniform manner along the vertical direction.

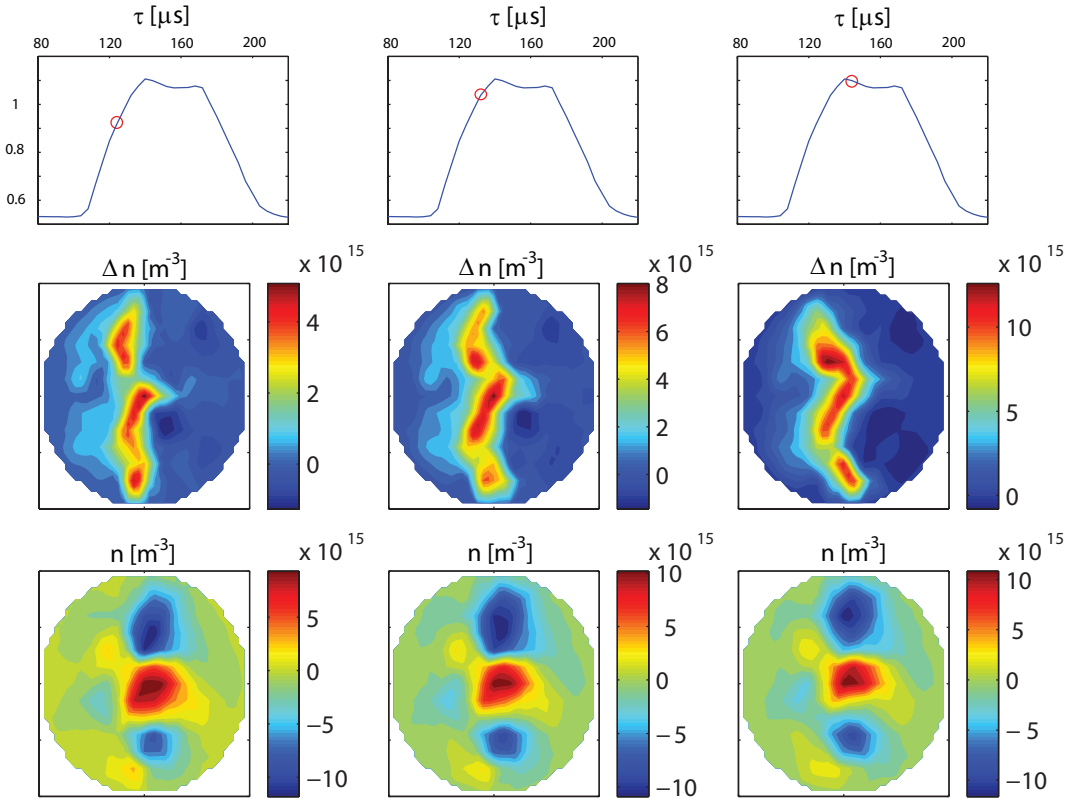

Figure 4.22: For three instants, the difference between the CS-result with and without pulses (middle row) as well as the result for the triggers without micro-pulses (bottom row) is shown. In the top row, the CS-averaged microwave pulse is shown. The time of the shown frames with respect to the pulse is indicated by the red circle.

5

Conclusion and Outlook

This diploma thesis investigates blob ejection in the basic plasma physics experiment TORPEX. For this purpose, conditional sampling (CS) is extensively studied and applied to ion-saturation current measurements from the two-dimensional imaging probe HEXTIP. The observation of earlier experiments that blobs originate from the positive wave crest of a saturated interchange mode is verified with this diagnostic. In addition, the ejection of blobs from a more stable plasma configuration is observed. The relation between local density gradients and blobs is studied for both scenarios. In a first step, the evolution of the gradients leading to a blob ejection is studied by triggering on such events. The strongest gradients right before a first sign of growing of the instability in the CS-result are interpreted as possible candidates to cause the avalanche-like transport event. Their magnitude is seen to decrease for smaller blobs. In a further step, these gradients are used as reference signals for CS to determine their role in the dynamics leading to blobs. In the case where blobs are observed to originate from a slab like plasma configuration, two conditions on the plasma profile are found to have an enhanced probability to produce a blob. One is a strong gradient at a local position, the other one is a large vertically-averaged radial gradient. The latter is detected by the use of spatial Fourier transform. In the scenario where the gradient stems from a positive wave crest, a similar result is obtained. The probability for blob detection strongly depends on the magnitude of the radial density gradient at a position to the left of the mode. From the CS-profile at the instant of the trigger, it is argued that a large local gradient automatically indicates a large average gradient along the vertical direction. Two mechanisms leading to a growth of the radial gradient are suggested. One is the source, which is shown to lie mostly on the high field side of the mode, even for large mode amplitudes. A local increase is to be expected at the positions of negative wave crests, where an inward $\mathbf{E} \times \mathbf{B}$ drift is implied by structures of positive and negative potential observed in an earlier experiment.

With the $probability\ chart$, a new tool is introduced which allows a probabilistic evaluation

of the effect of different trigger conditions. It allows to circumvent the limitations of standard CS. The developed procedure and Matlab routines can immediately be used to study different configurations of the plasma, or the relation between blobs and other quantities, such as for example the amplitude of the mode or the radial gradient averaged along the vertical direction. This work could also serve as a basis for a similar investigation with measurements from a fast imaging camera recently installed on TORPEX, which is not subjected to a limited spatial resolution. In addition, the presented experimental results could be used for comparisons with numerical simulations of blob ejection, which are in progress and match more and more realistic scenarios on TORPEX.

Bibliography

[1] N. Bisai, A. Das, S. Deshpande, R. Jha, P. Kaw, A. Sen, and R. Singh. Formation of a density blob and its dynamics in the edge and the scrape-off layer of a tokamak plasma. *Phys. Plasmas*, 12, (2005).

[2] D. Block, I. Teliban, F. Greiner, and A. Piel. Prospectus and limitations of conditional averaging. *Phys. Scr.*, T122, (2006).

[3] S. Brunner. Waves and instabilities in inhomogeneous plasmas (course 3ème cycle). http://crppwww.epfl.ch/ brunner/inhomoplama.pdf.

[4] A. Fasoli, B. Labit, M. McGrath, S.H. Müller, G. Plyushchev, M. Podestà, and F.M. Poli. Electrostatic turbulence and transport in a simple magnetized plasma. *Phys. Plasmas*, 13, (2006).

[5] H.L. Johnsen, H.AND Pécseli and J. Trulsen. Conditional eddies in plasma turbulence. *Phys. Fluids*, 30(3), (1987).

[6] S. H. Müller, A. Diallo, A. Fasoli, I. Furno, B. Labit, and G. Plyushchev. Probabilistic analysis of turbulent structures from two-dimensional plasma imaging. *Phys. Plasmas*, 13, (2006).

[7] S. H. Müller, A. Fasoli, B. Labit, O. McGrath, G. Pisaturo, and G. Plyushchev. Basic turbulence studies on toroidal plasma experiment and challenges in theory-experiment comparison. *Phys. Plasmas*, 12, (2005).

[8] S.H. Müller. Turbulence in basic toroidal plasmas, September (2006).

[9] S.H. Müller, A. Fasoli, B. Labit, M. McGrath, M Podestà, and F.M. Poli. Effects of a vertical field on particle confinement in a magnetized plasma torus. *Phys. Rev. Lett.*, 93(16), (2004).

[10] Frank J. Øynes, Ole-Morten Olsen, Hans L. Pécseli, Fredriksen Åshild, and Kristoffer Rypdal. Experimental study of low-frequency electrostatic fluctuations in a magnetized toroidal plasma. *PHYSICAL REVIEW E*, 57(2), (1998).

[11] H.L. Pécseli, E.A. Coutsias, T. Huld, J.P. Lynov, A.H. Nielsen, and Juul J. Rasmussen. Coherent vortical structures in two-dimensional plasma turbulence. *Plasma Physics and Controlled Fusion*, 34(13), (1992).

[12] M. Podestà. Plasma production and transport in a simple magnetised toroidal plasma, February (2007).

[13] M. Podestà, A. Fasoli, B. Labit, M. McGrath, S. H. Müller, and F. M. Poli. Plasma production by low-filed side injection of electron cyclotron waves in a simple magnetized plasma. *Plasma Phys. Control. Fusion*, 47:1989–2002, (2005).

[14] F.M. Poli, S. Brunner, A. Diallo, A. Fasoli, I Furno, B. Labit, S.H. Müller, G. Plyushchev, and M Podestà. Experimental characterization of drift-interchange instabilities in a simple toroidal plasma. *Phys. Plasmas*, 13, (2006).

[15] K. Rypdal, A. Fredriksen, O.M. Olsen, and K.G. Hellbolm. *Phys. Plasmas*, 4, (1997).

[16] Y. Sarazin and Ph. Ghendrih. Intermittent particle transport in two-dimensional edge turbulence. *Phys. Plasmas*, 5(12), (1998).

[17] P. C. Stangeby. *The Plasma Boundary of Magnetic Fusion Devices*. Physics Publishing, Bristol and Philadelphia, (2000).

[18] U. Stroth, F. Greiner, C. Lechte, N. Mahdizadeh, K. Rahbarnia, and M. Ramisch. Study of edge turbulence in dimensionally similar laboratory plasmas. *Phys. Plasmas*, 11(5):2558–2564, (2004).

[19] J.A. Wesson. *Tokamaks*. Clarendon Press, Oxford, 3rd edition, (2004).